

# **Prediction of NMR Parameters and geometry in $^{133}\text{Cs}$ -containing compounds using Density Functional Theory**

N. Manukovsky<sup>1</sup>, N. Vaisleib<sup>1</sup>, M. Arbel-Haddad<sup>2</sup>, A. Goldbourt<sup>1</sup>

<sup>1</sup>School of Chemistry, Tel Aviv University, Ramat Aviv 6997801, Tel Aviv, Israel

<sup>2</sup>Nuclear Research Center Negev, PO Box 9001, Beer Sheva 84901, Israel

## Abstract

The need to immobilize low-level nuclear waste, in particular  $^{137}\text{Cs}$ -bearing waste, has led to a growing interest in geopolymer-based waste matrices, in addition to optimization attempts of cement matrix compositions for this specific application. Although the overall phase composition and structure of these matrices are well characterized, the binding sites of Cs in these materials have not been clearly identified. Recent studies have suggested that combining the sensitivity of solid-state Nuclear Magnetic Resonance (SSNMR) to the local atomic structure with other structural techniques provides insights into the mode of Cs binding and release. Density Functional Theory (DFT) can provide the connection between spectroscopic parameters and geometric properties. However, the reliability of DFT results strongly relies on the choice of a suitable exchange-correlation functional, which for  $^{133}\text{Cs}$ , the NMR surrogate for such studies, is not well-established. In this work we benchmark various functionals against their performance in predicting the geometry of various simple Cs compounds, their NMR quadrupolar coupling constants, and their chemical shift values. The results show rev-vdW-DF2 to be a leading, though not a flawless, candidate for these systems, and apparently for additional classes of Cs-containing systems.

## Introduction

Cesium is an alkali metal whose ionic form plays a key role in various materials and applications, including chemical catalysis<sup>1</sup>, purification of biological macromolecules<sup>2</sup>, and optoelectronic devices<sup>3</sup>. Radioisotopes of Cs, specifically  $^{137}\text{Cs}$ , a  $\beta$ -emitter with a half life time of  $\sim 30$  yrs, are found in low-level radioactive waste streams. The long term immobilization of Cs-bearing radioactive waste is a challenging task due to the high solubility of Cs ions in aqueous media. Cements<sup>4</sup> and geopolymers<sup>5</sup> are suitable for the immobilization of low-level radioactive waste due to their favorable ion-binding properties, low cost and ease of preparation, durability under irradiation, and stability. Geopolymer-based waste matrices have been specifically studied in for immobilization of Cs-bearing wastes, due to their ability to specifically bind Cs ions. Examples from recent years are the many studies regarding immobilization of incineration ashes from the Fukushima region, which have a high content of radioactive  $^{134}\text{Cs}$  and  $^{137}\text{Cs}$  following the nuclear accident in 2011. Alkaline activation of the ashes leads to the formation of geopolymeric wastefoms<sup>6-8</sup> consisting of various crystalline and amorphous phases. The ultimate Cs immobilizing matrix should be characterized by high Cs binding, and consequently minimal leaching to the environment under relevant environmental conditions. High-resolution structural characterization of Cs-bearing matrices, clarifying properties such as the binding site(s) geometry, the binding phase where several phases coexist, and the equilibrium distribution between competing sites, can contribute to the rational design of improved immobilization matrices. Parameters provided by solid-state NMR (SSNMR), such as chemical shift, dipolar coupling, and quadrupolar coupling, are sensitive to the local geometry of the studied nuclei, including its binding atoms, bond lengths and angles, and its non-covalent interactions with the environment. Thus, they

contain a wealth of local geometric and electronic structure information. However, only few examples show how  $^{133}\text{Cs}$  SSNMR can be utilized to characterize Cs binding sites<sup>9–15</sup> in porous matrices.

In general, there is no simple, straightforward method to directly infer structural properties from the NMR parameters unless the dipolar interaction, which is proportional to the inverse cube of the distance, is directly measured. First-principles calculations are known to bridge the gap between spectroscopy and structure, thus allowing to utilize the information content of SSNMR to its fullest. Density functional theory (DFT) has been in vast use in the physics and chemistry communities for decades, due to its ability to predict diverse properties, such as ground state structure, excitation energies, spectroscopic properties, reaction energies and more, for molecules and solids, with high accuracy and at a relatively modest computational cost. Specifically, the use of DFT calculations side by side with NMR measurements has become widespread since the introduction of the GIPAW (Gauge Including Projector Augmented Wave) method<sup>16–18</sup>, which provides the ability to compute NMR tensors in solid systems with all-electron accuracy. Although DFT has been helpful in the structural characterization of zeolites<sup>19,20</sup>,  $^{133}\text{Cs}$  has not been extensively studied using DFT-GIPAW. Relevant examples of the combination of  $^{133}\text{Cs}$  SSNMR and DFT are the study of Cs adsorption on Montmorillonite Clay<sup>11</sup>, and their use to study Cs-containing perovskites<sup>21</sup> and cryptands<sup>22</sup>.

Prior to the use of DFT-GIPAW for probing Cs binding in complex systems such as cements and geopolymers, which are often a conglomerate of several crystalline and non-crystalline phases, it is instructive to screen the suitability of different DFT functionals to correctly predict  $^{133}\text{Cs}$  NMR parameters using simpler, well characterized Cs-containing systems. Cs-halides (CsF, CsCl, CsBr, and CsI) are the obvious place to start. Experimentally, it is well known that under ambient temperature and pressure, CsF crystallizes in the B1 phase, forming the so called NaCl or rock-salt structure, as most alkali halides do. However, CsCl, CsBr, and CsI crystallize in the B2 phase (Figure 1), being the only alkali halides known to crystallize in the so-called CsCl structure under these conditions<sup>23</sup> (the discussion omits Fr and At, about which no data is available)<sup>24</sup>. The reason for this difference is dispersion interactions which favor the phase with the shorter distances between ions of the same kind, that is, the CsCl phase. These interactions depend on the ion polarizability, and are therefore more substantial in the mentioned systems consisting of heavy ions<sup>25,26</sup>. Van der Waals forces make only a minor contribution to the total lattice energy of an ionic lattice (1-5% of the lattice energy), but they are the factor determining the phase in this case<sup>26</sup>. Zhang et al.<sup>27</sup> have shown that despite the simplicity of cesium halide structures, the popular Perdew-Burke-Ernzerhof (PBE)<sup>28</sup> functional, commonly used for the prediction of NMR parameters for  $^{133}\text{Cs}$ <sup>11,21</sup> and other nuclei<sup>29–32</sup>, fails to predict the correct phase for CsCl. The same also occurs when using other GGA-type functionals such as the solid-state optimized PBEsol<sup>27</sup>, PW91 and revPBE<sup>33</sup>, as well as for various meta-GGA type functionals (MS0, MS1, MS2, TPSS and rTPSS)<sup>33</sup>. A plausible explanation is that pure DFT functionals do not include terms describing dispersion forces<sup>27,34</sup>. Pure DFT functionals are semilocal, meaning that the energy density at any point depends only on properties at that point. Consequently, these functionals are by definition unable to model dispersion, which is an interaction between instantaneous dipoles at two different sites. Indeed, the correct CsCl structure is obtained using calculation schemes incorporating dispersion<sup>27,35</sup>.

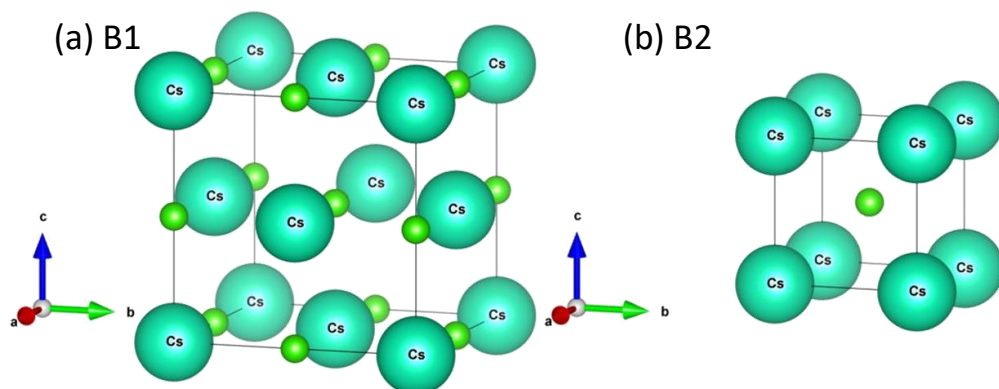


Figure 1: (a) B1 (NaCl) phase vs (b) B2 (CsCl) phase unit cells<sup>23</sup>. The large spheres represent the metal, whereas the small ones represent the halide. At room temperature, only CsF adopts the B1 phase.

Dispersive interactions can be introduced into DFT by various approaches<sup>34</sup>. A common approach is the addition of asymptotic dispersion corrections to the energy obtained by a standard DFT calculation, in the manner of an interatomic potential<sup>36–43</sup>. Notable examples of dispersion corrections are the Grimme schemes DFT+D<sup>36</sup>, DFT+D2<sup>37</sup> and DFT+D3<sup>44</sup>; Tkatchenko-Scheffler (TS) dispersion correction<sup>38</sup> and the subsequent Many-body dispersion (MBD) correction<sup>45</sup>, and Exchange-hole dipole-moment model (XDM)<sup>46–48</sup>. Asymptotic dispersion corrections can attain good accuracy at a relatively low computational cost, and can be applied in conjunction with various, well-tested functionals. Another approach is the development of explicitly non-local density functionals<sup>49–56</sup>, whereby the energy depends on the density and its gradient at two points in space simultaneously. Notable examples of non-local functionals are vdW-DF<sup>51</sup>, vdW-DF2<sup>54</sup>, vdW-DF3<sup>57</sup>, and rVV10<sup>52,55</sup>. Additional methods include dispersion-correcting potentials<sup>58–61</sup>, and parameterized exchange-correlation functionals<sup>62–64</sup>. Finally, meta-GGA functionals<sup>65,66</sup> can incorporate short-range, but not long-range, dispersion interactions through their dependence on the kinetic energy.

For Cs halides, forcing the right phase upon the popular PBE functional yields a good prediction of the chemical shift<sup>67</sup>, but does not solve the problem of the accurate geometry prediction. It is currently unknown which functional can correctly capture both the geometry and the NMR parameters of Cs-compounds, ranging from Cs halides to Cs-bearing Zeolites.

This work aims to identify the most suitable DFT scheme for the prediction of the correct geometry and NMR parameters of various Cs-containing systems. First, we screen various functionals for their ability to predict the correct phase in Cs halides. We then compare their performance in predicting the crystal unit cell volume, chemical shift and quadrupolar coupling constants in Cs halides, Cs oxyanions, and Cs-containing perovskites. Keeping in mind our interest in more computationally-demanding Cs-bearing materials, we have restricted this study to schemes of a reasonable computational cost. Differences in the performance and accuracy of various functionals, as well as their performance compared with experimental results available in the literature, are discussed, and recommendations for functional selection for the prediction of <sup>133</sup>Cs NMR parameters are proposed.

## Computational Methods

DFT calculations were carried out using the Quantum Espresso 7.1<sup>68,69</sup> software package, which uses the gauge-including projector augmented waves (GIPAW) method for computing magnetic resonance properties of crystalline structures. We used scalar relativistic PAW PBE or PBEsol pseudopotentials<sup>70</sup>, downloaded from the Quantum Espresso website. Spin-orbit coupling effects were found to be negligible and were not further considered (see SI table S13). The plane wave cutoff energies for eleven cesium-containing systems, determined by convergence tests, are listed in table S1 in the SI. The kinetic energy cutoff was four times that of the wave function. Monkhorst-Pack grids were used to sample the Brillouin zone (see table S1 for their dimensions), and the initial structures were taken to be the reported crystal structures (Table S2).

Various functionals and dispersion corrections were used for the calculations of geometry and NMR parameters. PBE<sup>28</sup>, known to fail in predicting the correct phase in cesium halides, is used as a reference, being a very common functional. Other GGA-type functionals examined here are revPBE<sup>71</sup>, a one-parameter modification of PBE; its further modification rPBE<sup>72</sup>, which performs well for the calculation of NMR parameters in solids containing elements of the third and fourth periods<sup>73,74</sup>; PBEsol<sup>75</sup>, tailored to solids; and B86bPBE<sup>28,76</sup>, the recommended functional to be paired with XDM for solid state calculations<sup>42</sup>. These five semilocal functionals are used as base functionals in conjunction with three dispersion corrections – DFT-D2<sup>37</sup>, DFT-D3<sup>44</sup>, and XDM<sup>48,77</sup>. PBE+MBD was not used as it is known to fail to converge for many cesium halides, and neither was PBE+TS which is known to yield the correct phase but provide incorrect lattice constants<sup>78</sup>. Non-local functionals considered are rVV10<sup>56</sup>, vdW-DF1<sup>51</sup>, vdW-DF2<sup>54</sup>, vdW-DF3<sup>57</sup>, vdW-DF-C6<sup>79</sup>, rev-vdW-DF2 (also called vdW-DF2-B86R)<sup>80</sup>.

Asymptotic dispersion corrections (such as D2, D3, and XDM) are implemented post-self-consistently, meaning they do not affect the electron density. Therefore, for a given geometric structure, the NMR properties, which strongly depend on the electronic structure, will be unaffected by these corrections. In contrast, nonlocal functionals are formulated self-consistently, directly influencing the electron density. However, all dispersion corrections of any type can indirectly affect any molecular property via their effect on the geometric structure. For this reason, we found it instructive to compare the NMR parameters obtained by different functionals using either the experimental (crystallographic) geometry or the DFT-optimized geometry, allowing us to distinguish between geometry-mediated effects and electronic-structure-mediated effects. In the cases where structural relaxation was implemented, both the lattice constants and the atomic positions were optimized using the BFGS algorithm, until the residual forces acting on each atom were below 1.0E-03 Ry/au.

## Results and Discussions

### Cesium halides polymorphs

Pure DFT functionals are known to fail in the prediction of the ground state structure of heavy Cs halides, owing to the absence of dispersion in the energy calculation. Therefore, the first criterion for DFT scheme screening was the ability to correctly predict the ground state phase, which is B1 for CsF

and B2 for heavier Cs halides. Unfortunately, the comparison to experiment is only qualitative, as the experimental values of the energy gap between Cs halides polymorphs are unavailable.

The results confirm that semilocal functionals erroneously assign the B1 phase to all Cs halides (Figure 2a). Interestingly, the slope of the energy gap curve is the same for all five GGA-type functionals tested here, with the exception of PBEsol for the CsF-CsCl segment. The addition of an asymptotic dispersion correction leads to the correct phase prediction in most, yet not all, combinations of base functionals (PBE, rPBE, revPBE, PBEsol, B86bPBE) and dispersion corrections (D2, D3, and XDM) tested here. The D2 correction (Figure 2b) using the default parameters leads to a non-physical trend where the energy gap is non-monotonous versus the halide size and was therefore not further used. Using Zhang's parameterization for Cs ( $C_6^{Cs} = 57.74 \frac{\text{Jnm}^6}{\text{mol}}$ ,  $R_0^{Cs} = 1.776 \text{ \AA}$ )<sup>27</sup> rectifies this. Using Schurko's D2\* reparameterization of the damping function<sup>81</sup> ( $d=3.25$  instead of the default 20), originally implemented using rPBE, on its own leads to a nearly flat curve and a wrong phase in CsF. Using Zhang's parameters together with Schurko's does not settle the phase issue and does not reproduce the trend with respect to the halide size. We note that D2\* was parametrized using the EFG tensors of three elements, and should in principle be transferrable to all elements. However, it was designed to provide a good fit of the EFG, not necessarily of the phase stability, and was trained on small organic molecules, very different from the inorganic salt structure studied here.

The D3 and XDM corrections (Figure 2c) lead in most cases tested here to the correct phase, although the trend is violated for PBE+D3, PBEsol+D3, and B86bPBE+XDM (the curves go slightly up from CsBr to CsI). A similar behavior was described for PBE+D3 with Li halides<sup>82</sup>. The energetic gap between the phases is larger for PBE (or PBEsol)+D2 than for PBE (or PBEsol)+D3. This can be explained by the fact that D2 describes dispersion using only two-body attractive interactions, whereas D3 also incorporates local environment effects and three-body repulsive interactions<sup>83</sup>.

All vdW-DF functionals tested (Figure 2d) yield curves of the same slope. Most of them yield the correct phase, as does rVV10. The hybrid functionals tested here do not capture the correct phase.

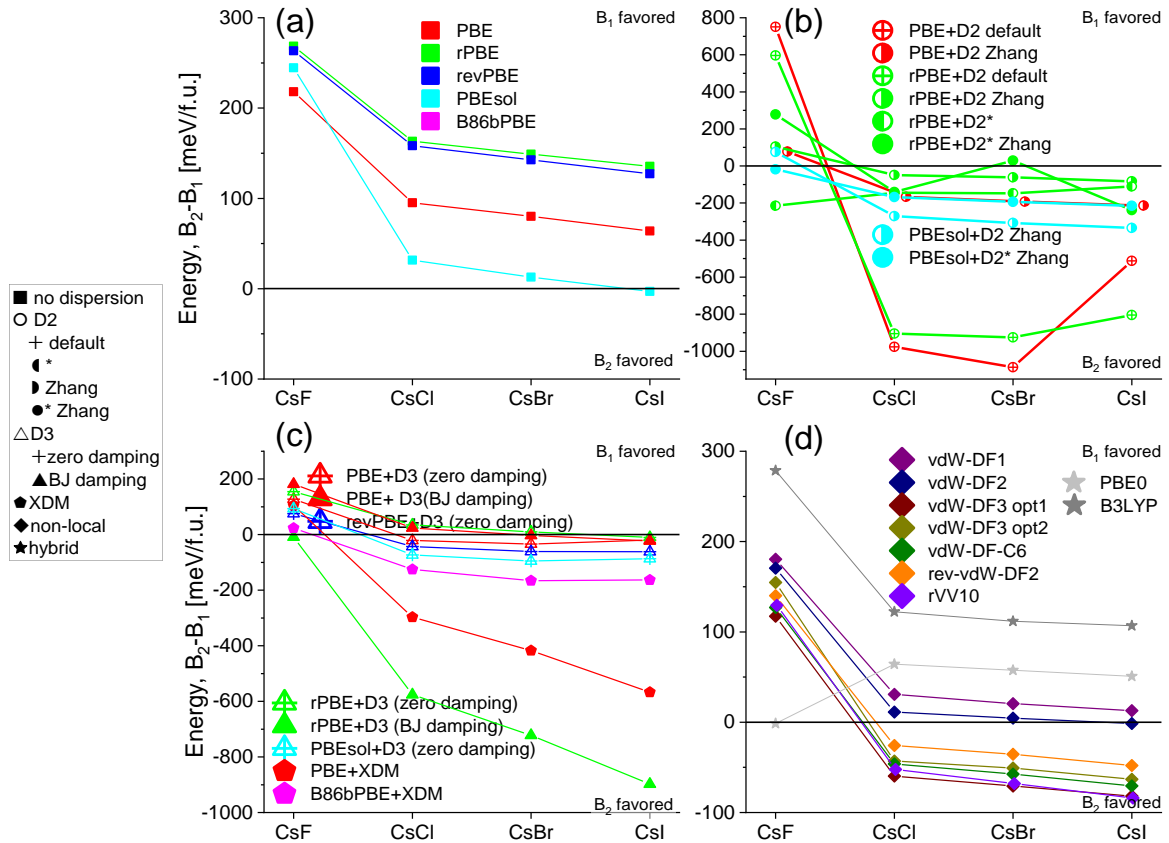


Figure 2: relative stability of Cs halide phases for various functionals: (a) semilocal functionals (■); (b) semilocal functionals with DFT-D2 dispersion correction (○; the symbol filling indicates the parametrization used); (c) semilocal functionals with DFT-D3 dispersion correction (△, the filling indicates the type of damping function used) or XDM (◆) dispersion correction; (d) non-local (◆) and hybrid (★) functionals.

The reliable structure prediction of Cs halides is challenging, since the energy gap between competing phases, caused by the typically weak dispersion forces<sup>26</sup>, is small, and is therefore very sensitive to errors arising in various approximations of the exchange-correlation energy. The energy gaps predicted here are similar to those calculated by Pyper (0.078 eV/f.u.)<sup>84</sup>, Aguado (0.14 eV/f.u.)<sup>85</sup>, and Zhang (0.16 eV/f.u.)<sup>27</sup>. As shown by others<sup>27</sup>, GGA and hybrid functionals fail to predict the correct phase of Cs halides. We therefore chose to proceed with non-local and dispersion-corrected semilocal functionals.

### Unit cell volume

In the next step of this study the ability of different functionals to predict the unit cell volume of Cs compounds was tested. The panel of Cs-compounds was expanded to include additional systems, namely four Cs oxyanions salts and three CsGeX<sub>3</sub> perovskites in addition to the four Cs halides studied thus far. Figure 3 features unit-cell volumes obtained from X-ray diffraction (literature values) and calculated unit cell volumes obtained using various DFT schemes, along with the mean error (ME) for each functional. We note that the DFT results refer to 0 K, while the experimental structures were determined at or around room temperature.

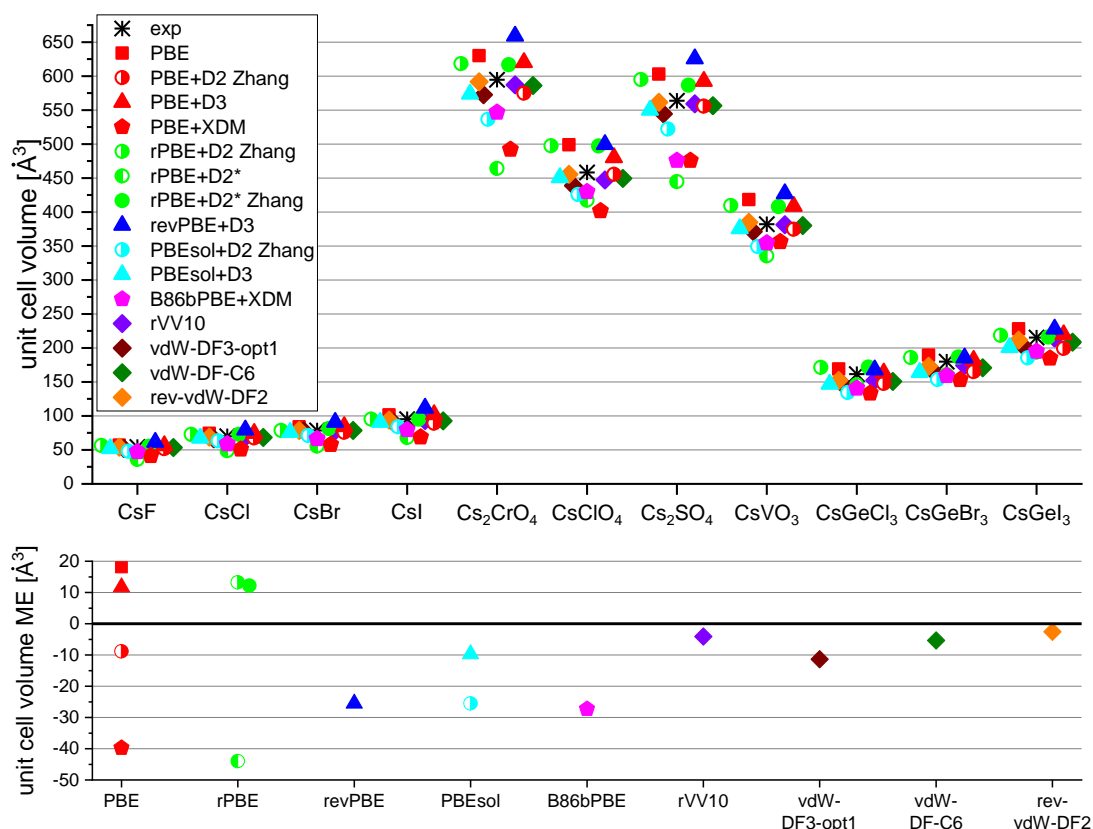


Figure 3: Unit-cell volume of various Cs-containing compounds as found experimentally by X-ray crystallography (asterisk) or by calculation using various DFT schemes. Some of the points are slightly horizontally shifted to avoid overlap. See table S2 for references of the experimental data. The bottom figures show the Mean Error (ME) of each functional. The mean relative error (MRE) and the coordinates root-mean-square-error (RMSE) are found in figure S1.

All schemes give a reasonable prediction of the unit cell volume, and correctly capture the trend among different compounds. Quantitatively, however, there are differences between various schemes. As expected, PBE overestimates the unit-cell volume. Adding a dispersion correction to PBE results, as expected, in a contraction of the calculated unit cell, to an extent that depends on the type of dispersion correction used. D2 is superior to XDM and D3 in this context, with XDM leading to an underestimation of the cell volume. The functionals revPBE+D3 and B86bPBE+XDM are outperformed even by uncorrected PBE. This is in contrast to the good performance of B86bPBE-XDM in predicting the lattice constant of the entire series of alkali halides<sup>86</sup>. This may be related to the fact that unlike the former study<sup>86</sup>, the current work includes compound containing polyatomic anions. Good performance is also displayed by the non-local functionals, as well as by rPBE+D2\* Zhang parametrization and PBEsol+D3.

### <sup>133</sup>Cs NMR parameters: The quadrupolar coupling constant

The calculation of the <sup>133</sup>Cs quadrupolar coupling constant  $C_q$ , using GIPAW and the same DFT schemes, is shown in Figure 4. A great difference is noticeable between different compounds: some are very sensitive to the calculation scheme (e.g. CsClO<sub>4</sub>, CsVO<sub>3</sub>), whereas some are not (e.g. CsGeX<sub>3</sub>, Cs<sub>2</sub>CrO<sub>4</sub> site 2, Cs<sub>2</sub>SO<sub>4</sub> site 1). This observation highlights the importance of screening a large sample of materials before choosing which calculation scheme to use.

PBE, though not accounting for dispersion and not providing an accurate unit cell volume (Figure 3), provides a very good prediction of the  $C_q$  parameter, slightly outperformed only by PBE+D3 and rPBE+D2\* Zhang. Adding D2 or XDM to PBE leads to an overestimation of  $|C_q|$ , although PBE+D2 yields good geometry (Figure 3). The other combinations of a GGA functional with an asymptotic dispersion correction are not better in terms of absolute error, but adding Grimme's D3 correction improves the relative error. All four non-local functionals yield similar results, and are all inferior to PBE and to PBE+D3, although their unit cell volume prediction was better (Figure 3).

Interestingly, when using the experimental geometry without geometry optimization (empty squares), all schemes tested here provide nearly identical results. It is not surprising that the semilocal functionals provide results similar to each other, as do the non-local functionals. However, it is not obvious that these two different families of functionals provide results similar to each other, despite the fact that dispersion is inherent in the non-local functionals, while this is not the case in the corrected ones. We therefore conclude that the main effect determining the accuracy of  $C_q$  here is the geometric structure, not the difference in the functional itself. This is in agreement with other studies<sup>87</sup>. However, remarkably, the functionals excelling at geometry prediction (e.g. rVV10, rev-vdW-DF2) do not excel at  $C_q$  prediction, showing that the structure most similar to the experimental one is not necessarily the one leading to the best  $C_q$ , at least for the type of Cs compounds studied here. Moreover, geometry optimization often results in a higher deviation the  $C_q$  prediction from the experimental value, with the exception being uncorrected PBE, PBE+D3, and rPBE+D2\* Zhang parameterization.

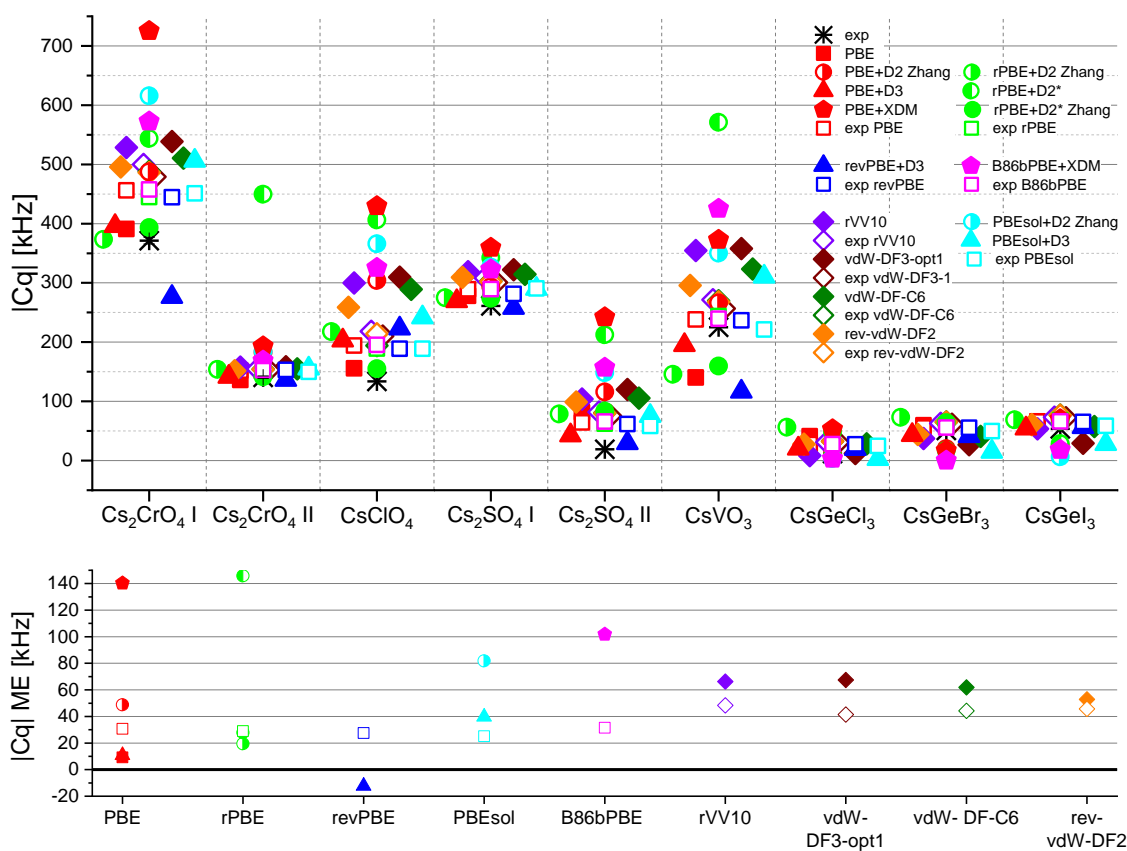


Figure 4: Quadrupolar coupling constant  $C_q$  of various Cs compounds. The black asterisk corresponds to the experimental value (table S3), whereas the colored symbols correspond to computational results. Solid symbols represent calculations



where the geometry was optimized, whereas open symbols correspond to calculations employing the experimental (XRD) geometry). The bottom plot shows the mean error in Cq. Additional error metrics are given in figure S1.

An important aspect in the analysis of  $^{133}\text{Cs}$ , is that in many materials of interest the experimental value of its quadrupolar coupling constant is small, and its experimental measurement is therefore difficult also due to its high spin ( $S=7/2$ ), leaving the chemical shift, which has a relatively broad ppm range, to be the most informative  $^{133}\text{Cs}$  NMR observable. We therefore turn to calculations of  $^{133}\text{Cs}$  shifts.

### $^{133}\text{Cs}$ NMR parameters: Chemical shifts

We have used DFT calculations to predict the  $^{133}\text{Cs}$  chemical shielding tensor. To convert the absolute shielding to the chemical shift, we plotted in Figure 5a the calculated isotropic shieldings versus the experimental isotropic shifts. Experimental values have been obtained from various literature sources, as shown and referenced in Table S 8, as well as experiments performed in our lab. A literature review revealed that for the simple Cs salts we analyzed, different reference compounds have been used and occasionally spectral referencing was not clearly stated.  $^{133}\text{Cs}$  chemical shifts are known to be concentration dependent<sup>88</sup>, and the use of CsCl solutions as an external reference must be done with care. The commonly cited manuscript by Haase<sup>89</sup>, performed on static samples and at a low field (2.1T), reports that a solution of 0.5m CsCl resonates at +6.1 ppm with respect to infinite dilution, and that solid CsCl is at 228.1 ppm. A later study by Mooibroek<sup>90</sup> reports solid CsCl to be +223.2 ppm with respect to 0.5m CsCl, and this value is more commonly used in the literature, although some studies also use a 1M CsCl solution. Our experimental data, measured under 5 kHz magic-angle spinning at a field of 14.1T, shown in Figure S4, allowed us to reconcile the seemingly contradicting literature results, setting a uniform reference scale. We used solid CsCl as a reference at +223.2 ppm, obtained that a 1M CsCl solution has a chemical shift of 5.0 ppm, and from several solutions of CsCl the infinite dilution chemical shift value is projected to -6.1 ppm, in agreement with Haase and the correction by Mooibroek for solid samples. All experimental values obtained from the literature were therefore re-referenced using the corrected scale.

The correlations between the re-referenced experimental chemical shifts and calculated chemical shielding, presented in Figure 5a, reveal that most calculation schemes are well fitted by linear curves, with the exception being rPBE+D2\*. However, the slopes differ from the ideal value of -1 (Figure 5). The greatest deviations from the ideal slope are those of XDM corrected functionals and of rPBE+D2\*, the latter being greatly improved by adding Zhang's parametrization along with that of D2\*. The slopes closest to -1 are those of revPBE+D3 (-0.90±0.03) and PBE+D3 (-1.18±0.04). Most other functionals feature slopes in the range [-1.45, -1.2], the differences between most functionals being insignificant, even when comparing, for example, between uncorrected semilocal functionals using the experimental geometry and non-local ones including geometry optimization.

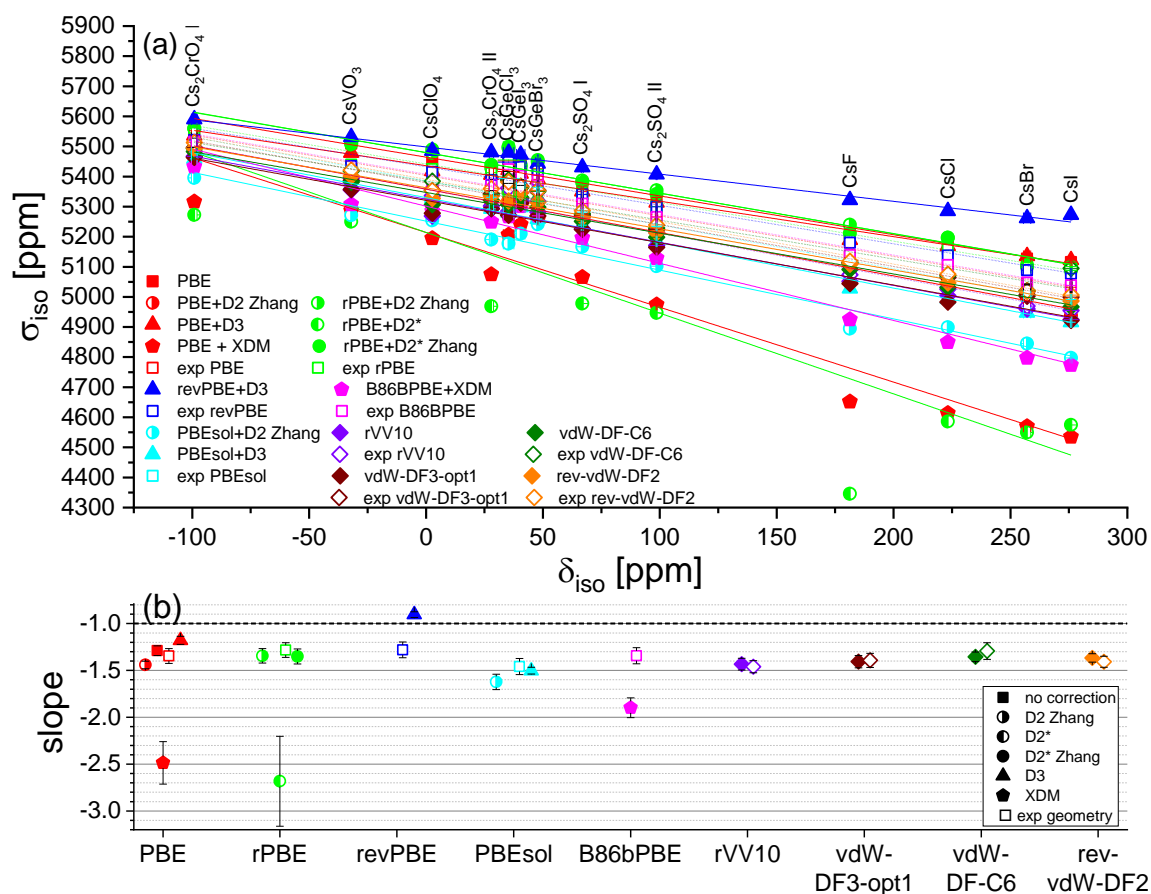


Figure 5: (a) Linearization plots of the isotropic shielding of various schemes and (b) their corresponding slopes. The error bars of the slopes are mostly smaller than the symbol sizes.  $\delta_{\text{iso}}$  are averaged experimental results collected from the literature (re-referenced) and from our own measurements (Table S8 and Figure S4).

We used the fitted correlations to convert the calculated chemical shieldings to shifts. The results, plotted in Figure 6, show that all functionals capture the general trend in the chemical shift of different systems. However, quantitative accuracy differs between different schemes. When using the experimental geometry, the shift is nearly independent of functional, as reported in other studies<sup>91</sup>, and as we observed in the prediction of Cq. Geometry optimization improves the accuracy for most schemes, in contrast to the case of Cq calculation. While for experimental geometry the Mean Absolute Error (MAE) of  $\delta_{\text{iso}}$  values is mostly between 15-20 ppm (empty symbols), the best accuracy after optimization is achieved by PBEsol+D3 (MAE=6.2 ppm), rev-vdW-DF2 (8.9), PBE+D2 (9.7), revPBE+D3 (10.4), PBE+D3 (10.5), rVV10 (10.8), and vdW-DF-C6 (10.9). These MAE's amount to 3% of the total shift span (372 ppm). Interestingly, it has been shown that PBE+D3 does not perform well in the calculation of  $^{13}\text{C}$  chemical shift in zeolites<sup>91</sup>, whereas PBEsol+D3 is usually not used for chemical shift calculations.

To distinguish between a systematic tendency rather than a random error in the estimation of the chemical shift, we also show the Mean Signed Error in figure S1. For all tested functionals, the MSE is practically zero, indicating a random error.

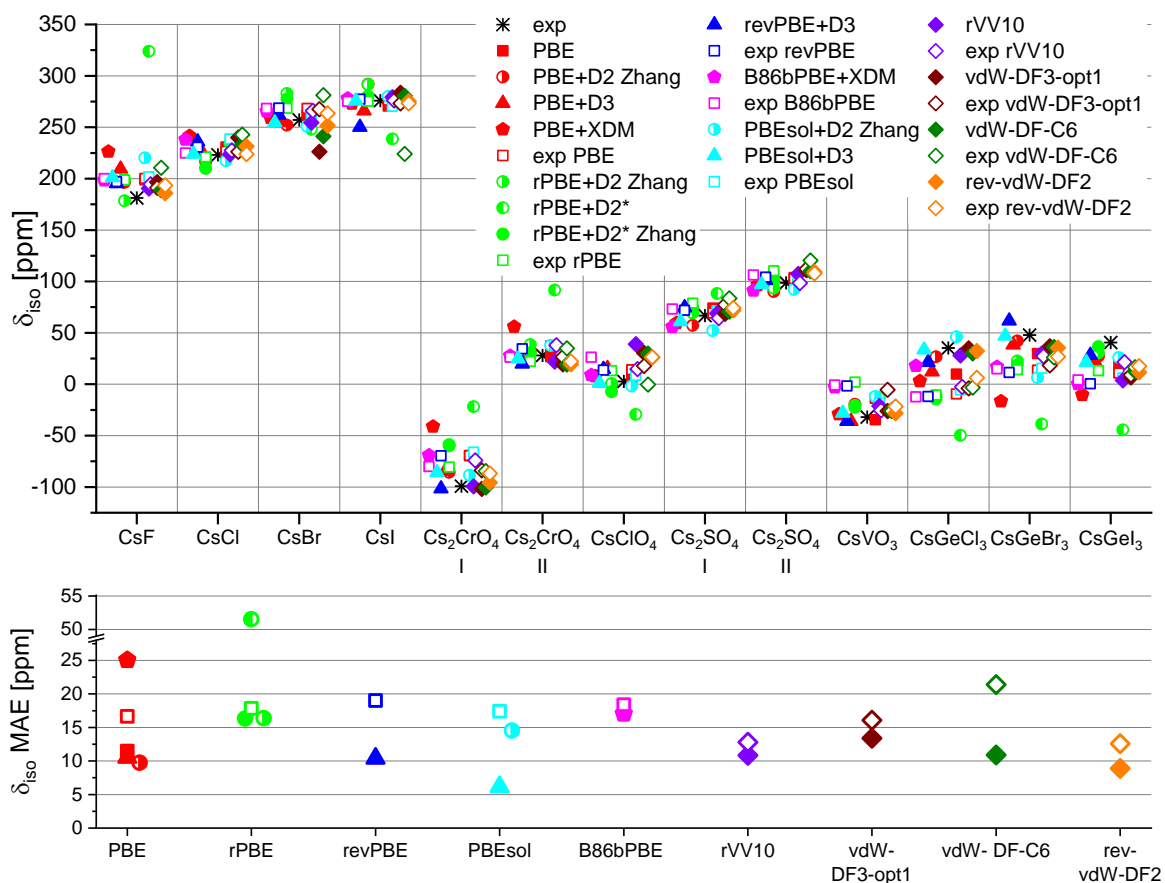


Figure 6: Computational and experimental values of the isotropic chemical shifts for various Cs compounds measured by us (figure S 4) and others (see table S8 for references). The bottom plot shows the mean absolute error in  $\delta_{\text{iso}}$ . An additional error metric is found in figure S1.

When zooming in on a more subtle trend, that of the isotropic chemical shift versus the halide size (Figure 7), and observing the apparently best functionals for the chemical shift prediction, it can be seen that revPBE+D3 fails to predict the trend in CsI, whereas rev-vdW-DF2 and PBEsol+D3, which were successful for the Cs halides, fail in CsGeX<sub>3</sub> (note that the parabolic shape, where the maximum is at Br, is kept). Only PBE+D3 qualitatively captures the halide trends in both series.

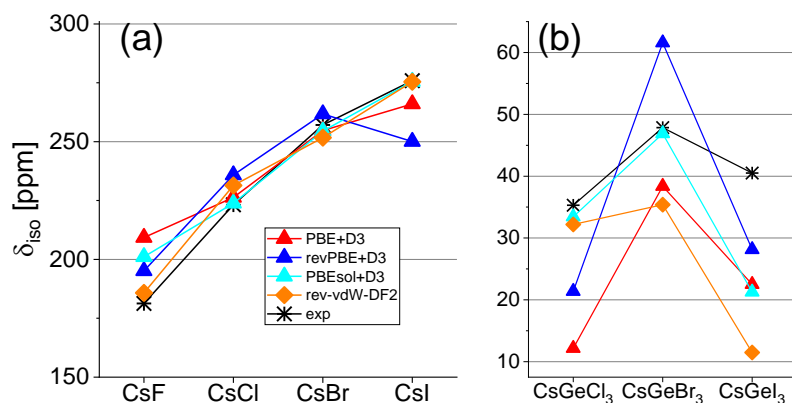


Figure 7: Isotropic chemical shifts for (a) Cs halides and (b) Perovskites (Cesium Germanium halides).

Chemical shift anisotropy (CSA) values have also been calculated for the various materials (shown in figure S5 in the SI), and were found to be insensitive to the functional used for most studied systems.

## Overall performance of functionals in this study

The mean errors of all functionals (including geometry optimization) for the unit cell volume, isotropic shift, and quadrupolar coupling constant are summarized in Figure 8.

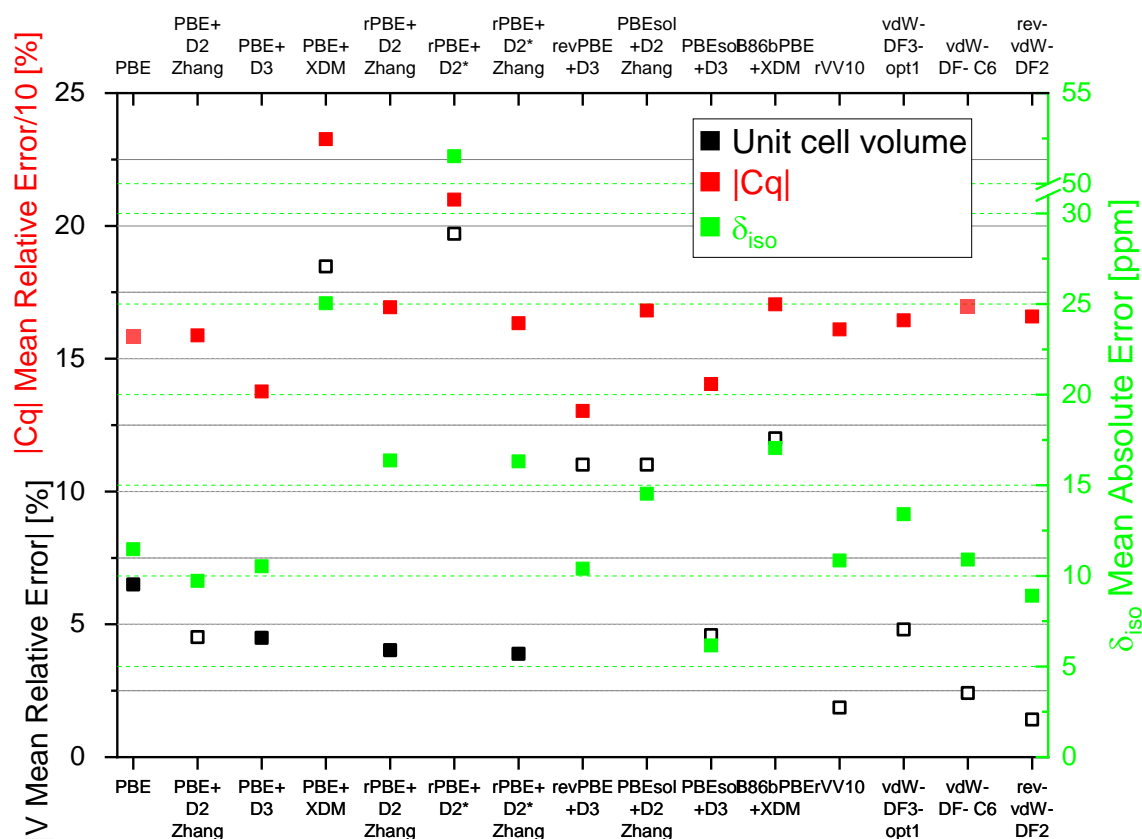


Figure 8: MRE of the unit cell volumes (black, empty squares are for negative values), MAE of the isotropic chemical shifts (green), and MRE of the quadrupolar coupling constants (red) for all schemes.

PBE characteristically overestimates the unit cell volume, while providing good (yet not the best) NMR parameters. Adding the D2 correction leads to an underestimation of the cell volume while marginally improving the accuracy of the chemical shift. Adding the D3 correction to PBE leads to very good overall performance, among the best in each of the three observables. XDM correction to PBE or B86bPBE, leads to a major underestimation of the cell volume, as well as to poor chemical shift prediction. rPBE+D2, using Zhang’s parametrization for Cs, provides good accuracy in the geometry, but not in the NMR parameters. Schurko’s D2\* parametrization has a marginal effect only. Interestingly, PBEsol+D2 fails in the geometry, but performs well for the NMR parameters. Likewise, revPBE+D3 fails in the geometry, but surprisingly excels in Cq prediction, while performing well for the shift. PBEsol+D3 performs very well, among the best, for the volume and the quadrupolar coupling, and excels in chemical shift. Its overall performance is among the best.

rVV10, vdW-DF-C6 and rev-vdW-DF2 excel at the unit cell prediction, while performing among the best in the chemical shift, and provide reasonably good quadrupolar coupling constants. vdW-DF3-opt1 is slightly inferior to them.

To sum up, this panel shows PBE+D3, PBEsol+D3, rVV10, vdW-DF-C6 and rev-vdW-DF2 to display good overall performance in predicting the geometry and NMR parameters of Cs salts, oxyanions and perovskites.

### Cs encaged in [2,2,2]-cryptand

To examine whether the results obtained using Cs salts, oxyanions and perovskites are transferrable to different Cs-containing systems, we applied the best performing functionals to a very different system,  $[\text{Cs}^+(\text{Cryptand}[2.2.2])\text{I}^-]$  (see inset of *Figure 9* for structure<sup>92</sup>). Unlike the ionic system studied here, in this system the Cs interacts with electronegative atoms (O, N) in the altogether neutral complex via ion-dipole interactions, forming a stable coordination complex encapsulating the metal in a spheroidal cavity, somewhat analogously to Cs binding to zeolites, although with shorter Cs-O distances. Here again we examine the prediction of unit cell volume, the quadrupolar coupling constant, and the isotropic chemical shift.

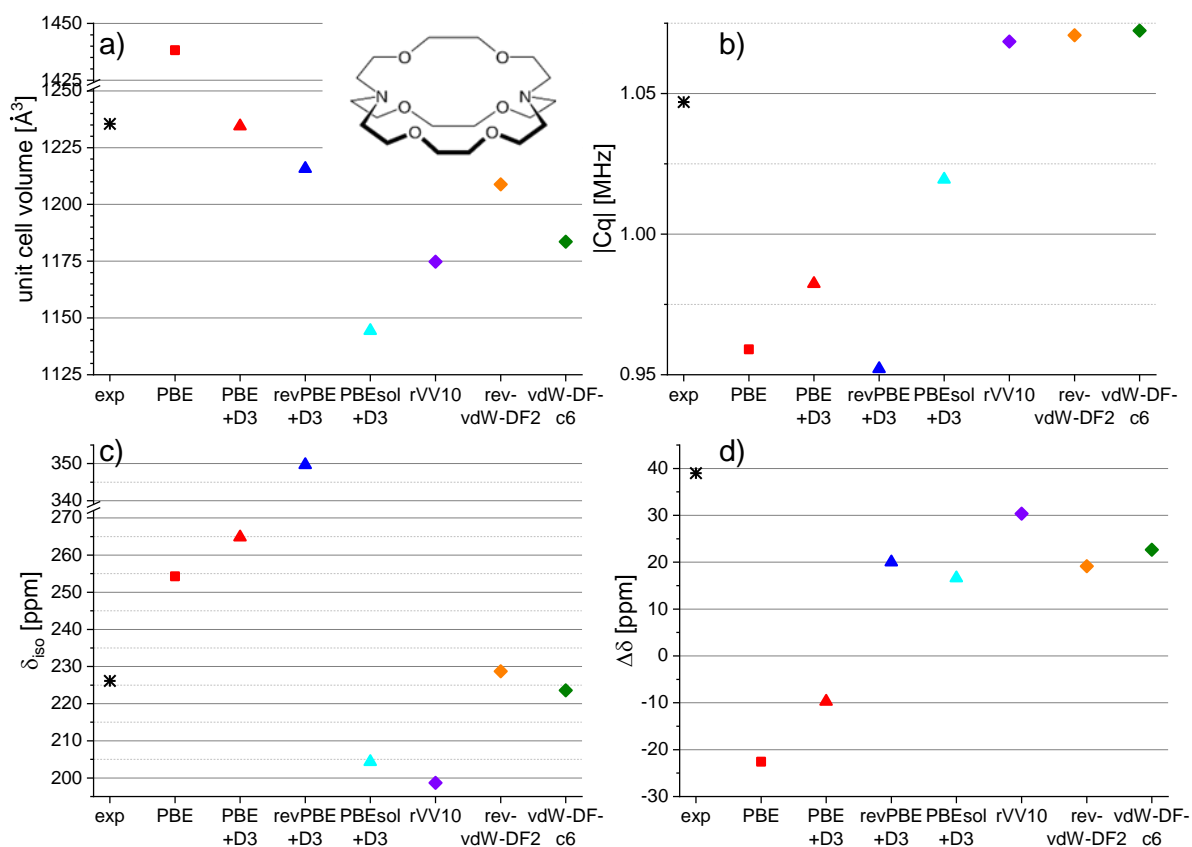


*Figure 9: a) Unit cell volume, b) Cq, c)  $\delta_{\text{iso}}$  and d) CSA of  $^{133}\text{Cs}$  in [2.2.2]Cryptand. The experimental unit cell volume and Cq are taken from ref<sup>22</sup>, and the experimental chemical shift is the average of values taken from<sup>22,93</sup>.*

As shown in Figure 9, here again the PBE functional overestimates the unit cell volume, while performing reasonably well (but not the best) in the NMR parameters. PBE+D3 excels in the geometry, even more than the non-local functionals, in contrast to the results with inorganic Cs compounds (Figure 3), while being mediocre in NMR parameters, again in contrast to the previous results (Figure 4, Figure 6). revPBE+D3 shows the largest error in both NMR parameters, despite a relatively good geometry prediction, again unlike the previous results. PBEsol+D3 performs poorly with the geometry

and is mediocre in NMR parameters, again in contrast to the previous part of this study, where PBEsol+D3 was among the best performers. All non-local functionals tested here excel at the Cq prediction, but specifically rev-vdW-DF2 outperforms them in unit cell volume and chemical shift, closely followed by vdW-DF-c6. Rev-vdW-DF2<sup>80</sup> has previously been shown to successfully predict the structural, mechanical, cohesive and vibrational properties of both weakly and strongly bound solids<sup>94</sup>, as well as the interlayer binding energy of multilayered solids<sup>95</sup> and the adsorption energy of adsorbed molecules<sup>96,97</sup>. It is however not yet widely used for chemical shift prediction<sup>98</sup>, and we are unaware of Cq calculations using this functional.

To conclude, switching from small systems to [2.2.2] cryptand, of all the functionals tested here, only rev-vdW-DF2 maintains its overall good performance and relative advantage. While we cannot determine if this conclusion holds for other cryptands, or to other materials, this functional appears to be a promising choice for the determination of Cs geometry and NMR parameters.

## Summary & Conclusions

A series of DFT functionals were screened for their performance and accuracy in the prediction of the geometry, quadrupolar coupling constants, and chemical shifts of cesium-133 in Cs-based halides, oxyanions and perovskites. The functionals chosen were those considering dispersive interactions, in order to faithfully predict the phase of Cs halides, while keeping a low computational cost. The best performing functionals, chosen mainly based on their performance with respect to geometry and isotropic chemical shift predictions, were then tested on a Cs-cryptand, which is structurally different than the above-mentioned inorganic compounds, and exhibits interactions of the Cs cation with polar groups, resembling to some extent Cs caged in zeolites. The results suggest that only one of the functionals tested, rev-vdW-DF2, maintained its advantage. Further work should be dedicated to the implementation of these functionals to the more challenging systems such as zeolites or geopolymers, used for the sequestration and immobilization of radioactive Cs species. More advanced (and computationally more expensive) meta-GGA and various hybrid functionals, possibly in combination with dispersion corrections may also be considered for these structurally complex systems.

## References

- (1) Jagadeeswaraiyah, K.; Balaraju, M.; Prasad, P. S.; Lingaiah, N. Selective Esterification of Glycerol to Bioadditives over Heteropoly Tungstate Supported on Cs-Containing Zirconia Catalysts. *Appl. Catal. Gen.* **2010**, *386* (1–2), 166–170.
- (2) Bachrach, U.; Friedmann, A. Practical Procedures for the Purification of Bacterial Viruses. *Appl. Microbiol.* **1971**, *22* (4), 706–715.
- (3) Bella, F.; Renzi, P.; Cavallo, C.; Gerbaldi, C. Caesium for Perovskite Solar Cells: An Overview. *Chem. Eur. J.* **2018**, *24* (47), 12183–12205.
- (4) Glasser, F. P. Progress in the Immobilization of Radioactive Wastes in Cement. *Cem. Concr. Res.* **1992**, *22* (2–3), 201–216.
- (5) Khalil, M.; Merz, E. Immobilization of Intermediate-Level Wastes in Geopolymers. *J. Nucl. Mater.* **1994**, *211* (2), 141–148.
- (6) Hong, S.-Y.; Glasser, F. P. Alkali Binding in Cement Pastes. *Cem. Concr. Res.* **1999**, *29* (12), 1893–1903. [https://doi.org/10.1016/S0008-8846\(99\)00187-8](https://doi.org/10.1016/S0008-8846(99)00187-8).
- (7) Xu, H.; van Deventer, J. S. J. Microstructural Characterisation of Geopolymers Synthesized from Kaolinite/Stilbite Mixtures Using XRD, MAS-NMR, SEM/EDX, TEM/EDX and HREM. *Cem. Concr. Res.* **2002**, *32*, 1705–1716.

- (8) Komnitsas, K.; Zaharaki, D. Geopolymerisation: A Review and Prospects for the Minerals Industry. *Miner. Eng.* **2007**, *20* (14), 1261–1277. <https://doi.org/10.1016/j.mineng.2007.07.011>.
- (9) Ahn, M. K.; Iton, L. E. Solid-State Cesium-133 NMR Studies of Cations in Cesium/Lithium/Sodium Zeolite A: An Example of Cation Dynamics Involving Three Sites. *J. Phys. Chem.* **1991**, *95* (11), 4496–4500. <https://doi.org/10.1021/j100164a059>.
- (10) Ashbrook, S. E.; Whittle, K. R.; Le Polles, L.; Farnan, I. Disorder and Dynamics in Pollucite from <sup>133</sup>Cs and <sup>27</sup>Al NMR. *J. Am. Ceram. Soc.* **2005**, *88* (6), 1575–1583. <https://doi.org/10.1111/j.1551-2916.2005.00294.x>.
- (11) Ohkubo, T.; Okamoto, T.; Kawamura, K.; Guégan, R.; Deguchi, K.; Ohki, S.; Shimizu, T.; Tachi, Y.; Iwadate, Y. New Insights into the Cs Adsorption on Montmorillonite Clay from <sup>133</sup>Cs Solid-State NMR and Density Functional Theory Calculations. *J. Phys. Chem. A* **2018**, *122* (48), 9326–9337. <https://doi.org/10.1021/acs.jpca.8b07276>.
- (12) Arbel-Haddad, M.; Harnik, Y.; Schlosser, Y.; Goldbourt, A. Cesium Immobilization in Metakaolin-Based Geopolymers Elucidated by <sup>133</sup>Cs Solid State NMR Spectroscopy. *J. Nucl. Mater.* **2022**, *562*, 153570. <https://doi.org/10.1016/j.jnucmat.2022.153570>.
- (13) Lambregts, M. J.; Frank, S. M. Characterization of Cesium Containing Glass-Bonded Ceramic Waste Forms. *Microporous Mesoporous Mater.* **2003**, *64* (1–3), 1–9. [https://doi.org/10.1016/S1387-1811\(03\)00486-4](https://doi.org/10.1016/S1387-1811(03)00486-4).
- (14) Ibarra, I. A.; Lima, E.; Loera, S.; Bosch, P.; Bulbulian, S.; Lara, V. II. Cesium Leaching in CsA and CsX Zeolites: Use of Blocking Agents to Inhibit the Cesium Cation Mobility. *J. Phys. Chem. B* **2006**, *110* (42), 21086–21091. <https://doi.org/10.1021/jp061926h>.
- (15) Norby, P.; Poshni, F. I.; Gualtieri, A. F.; Hanson, J. C.; Grey, C. P. Cation Migration in Zeolites: An in Situ Powder Diffraction and MAS NMR Study of the Structure of Zeolite Cs(Na)–Y during Dehydration. *J. Phys. Chem. B* **1998**, *102* (5), 839–856. <https://doi.org/10.1021/jp9730398>.
- (16) Pickard, C. J.; Mauri, F. All-Electron Magnetic Response with Pseudopotentials: NMR Chemical Shifts. *Phys. Rev. B* **2001**, *63* (24), 245101.
- (17) Charpentier, T. The PAW/GIPAW Approach for Computing NMR Parameters: A New Dimension Added to NMR Study of Solids. *Solid State Nucl. Magn. Reson.* **2011**, *40* (1), 1–20.
- (18) Bonhomme, C.; Gervais, C.; Babonneau, F.; Coelho, C.; Pourpoint, F.; Azais, T.; Ashbrook, S. E.; Griffin, J. M.; Yates, J. R.; Mauri, F. First-Principles Calculation of NMR Parameters Using the Gauge Including Projector Augmented Wave Method: A Chemist’s Point of View. *Chem. Rev.* **2012**, *112* (11), 5733–5779.
- (19) Schroeder, C.; Hansen, M. R.; Koller, H. Spatial Proximities between Brønsted Acid Sites, AlOH Groups, and Residual NH<sub>4</sub><sup>+</sup> Cations in Zeolites Mordenite and Ferrierite. *J. Phys. Chem. C* **2023**, *127* (1), 736–745.
- (20) Dib, E.; Mintova, S.; Vayssilov, G. N.; Aleksandrov, H. A.; Carravetta, M. Chemical Shift Anisotropy: A Promising Parameter to Distinguish the <sup>29</sup>Si NMR Peaks in Zeolites. *J. Phys. Chem. C* **2023**, *127* (22), 10792–10796.
- (21) Hooper, R. W.; Ni, C.; Tkachuk, D. G.; He, Y.; Terskikh, V. V.; Veinot, J. G.; Michaelis, V. K. Exploring Structural Nuances in Germanium Halide Perovskites Using Solid-State <sup>73</sup>Ge and <sup>133</sup>Cs NMR Spectroscopy. *J. Phys. Chem. Lett.* **2022**, *13* (7), 1687–1696.
- (22) Moon, C. J.; Park, J.; Im, H.; Ryu, H.; Choi, M. Y.; Kim, T. H.; Kim, J. Chemical Shift and Second-Order Quadrupolar Effects in the Solid-State <sup>133</sup>Cs NMR Spectra of [Cs<sup>+</sup> (Cryptand [2.2. 2])] X (X= I<sup>-</sup>, SCN<sup>-</sup>, H<sub>2</sub>O). *Bull. Korean Chem. Soc.* **2020**, *41* (7), 702–708.
- (23) Toledano, P.; Knorr, K.; Ehm, L.; Depmeier, W. Phenomenological Theory of the Reconstructive Phase Transition between the NaCl and CsCl Structure Types. *Phys. Rev. B* **2003**, *67* (14), 144106.
- (24) Posnjak, E.; Wyckoff, R. W. The Crystal Structures of the Alkali Halides. II. *J. Wash. Acad. Sci.* **1922**, *12* (10), 248–251.
- (25) Mayer, J. E. Dispersion and Polarizability and the van Der Waals Potential in the Alkali Halides. *J. Chem. Phys.* **1933**, *1* (4), 270–279.

- (26) London, F. The General Theory of Molecular Forces. *Trans. Faraday Soc.* **1937**, *33*, 8b–26.
- (27) Zhang, F.; Gale, J.; Uberuaga, B.; Stanek, C.; Marks, N. Importance of Dispersion in Density Functional Calculations of Cesium Chloride and Its Related Halides. *Phys. Rev. B* **2013**, *88* (5), 054112.
- (28) Perdew, J. P.; Burke, K.; Ernzerhof, M. Generalized Gradient Approximation Made Simple. *Phys. Rev. Lett.* **1996**, *77* (18), 3865.
- (29) Köcher, S. S.; Schleker, P.; Graf, M.; Eichel, R.-A.; Reuter, K.; Granwehr, J.; Scheurer, C. Chemical Shift Reference Scale for Li Solid State NMR Derived by First-Principles DFT Calculations. *J. Magn. Reson.* **2018**, *297*, 33–41.
- (30) Iwase, F. Ab Initio Calculations of Nuclear Quadrupole Resonance Frequencies in Trichloroacetyl Halides: A Comparison of DFT and Experimental Data. *Mater. Res. Express* **2020**, *7* (2), 025104.
- (31) Reina, J. V.; Civaia, F.; Harper, A. F.; Scheurer, C.; Köcher, S. The EFG Rosetta Stone: Translating between DFT Calculations and Solid State NMR Experiments. *Faraday Discuss.* **2024**.
- (32) Hartman, J. D.; Capistran, D. Predicting 51V Nuclear Magnetic Resonance Observables in Molecular Crystals. *Magn. Reson. Chem.* **2024**, *62* (6), 416–428.
- (33) Park, J.-S. Comparison Study of Exchange-Correlation Functionals on Prediction of Ground States and Structural Properties. *Curr. Appl. Phys.* **2021**, *22*, 61–64.
- (34) DiLabio, G. A.; Otero-de-la-Roza, A. Noncovalent Interactions in Density Functional Theory. *Rev. Comput. Chem.* **2016**, *29*, 1–97.
- (35) Grønbech, T. B. E.; Tolborg, K.; Ceresoli, D.; Iversen, B. B. Anharmonic Motion and Aspherical Nuclear Probability Density Functions in Cesium Halides. *Phys. Rev. B* **2022**, *105* (10), 104113.
- (36) Grimme, S. Accurate Description of van Der Waals Complexes by Density Functional Theory Including Empirical Corrections. *J. Comput. Chem.* **2004**, *25* (12), 1463–1473.
- (37) Grimme, S. Semiempirical GGA-type Density Functional Constructed with a Long-range Dispersion Correction. *J. Comput. Chem.* **2006**, *27* (15), 1787–1799.
- (38) Tkatchenko, A.; Scheffler, M. Accurate Molecular van Der Waals Interactions from Ground-State Electron Density and Free-Atom Reference Data. *Phys. Rev. Lett.* **2009**, *102* (7), 073005.
- (39) Steinmann, S. N.; Csonka, G.; Corminboeuf, C. Unified Inter- and Intramolecular Dispersion Correction Formula for Generalized Gradient Approximation Density Functional Theory. *J. Chem. Theory Comput.* **2009**, *5* (11), 2950–2958.
- (40) Steinmann, S. N.; Corminboeuf, C. Comprehensive Benchmarking of a Density-Dependent Dispersion Correction. *J. Chem. Theory Comput.* **2011**, *7* (11), 3567–3577.
- (41) Sun, Y.; Zhang, Z.; Grigoryants, V. M.; Myers, W. K.; Liu, F.; Earle, K. A.; Freed, J. H.; Scholes, C. P. The Internal Dynamics of Mini c TAR DNA Probed by Electron Paramagnetic Resonance of Nitroxide Spin-Labels at the Lower Stem, the Loop, and the Bulge. *Biochemistry* **2012**, *51* (43), 8530–8541.
- (42) Johnson, E. R. The Exchange-Hole Dipole Moment Dispersion Model. In *Non-covalent Interactions in Quantum Chemistry and Physics Theory and Applications*; de la Roza, A. O., DiLabio, G. A., Eds.; Elsevier, 2017; pp 169–194.
- (43) Caldeweyher, E.; Ehlert, S.; Hansen, A.; Neugebauer, H.; Spicher, S.; Bannwarth, C.; Grimme, S. A Generally Applicable Atomic-Charge Dependent London Dispersion Correction. *J. Chem. Phys.* **2019**, *150* (15), 154122.
- (44) Grimme, S.; Antony, J.; Ehrlich, S.; Krieg, H. A Consistent and Accurate Ab Initio Parametrization of Density Functional Dispersion Correction (DFT-D) for the 94 Elements H-Pu. *J. Chem. Phys.* **2010**, *132* (15), 154104.
- (45) Ambrosetti, A.; Reilly, A. M.; DiStasio, R. A.; Tkatchenko, A. Long-Range Correlation Energy Calculated from Coupled Atomic Response Functions. *J. Chem. Phys.* **2014**, *140* (18).
- (46) Becke, A. D.; Johnson, E. R. Exchange-Hole Dipole Moment and the Dispersion Interaction. *J. Chem. Phys.* **2005**, *122* (15), 154104.
- (47) Becke, A. D.; Johnson, E. R. A Density-Functional Model of the Dispersion Interaction. *J. Chem. Phys.* **2005**, *123* (15).



- (48) Otero-De-La-Roza, A.; Johnson, E. R. Van Der Waals Interactions in Solids Using the Exchange-Hole Dipole Moment Model. *J. Chem. Phys.* **2012**, *136* (17).
- (49) Andersson, Y.; Langreth, D. C.; Lundqvist, B. I. Van Der Waals Interactions in Density-Functional Theory. *Phys. Rev. Lett.* **1996**, *76* (1), 102–105. <https://doi.org/10.1103/PhysRevLett.76.102>.
- (50) Dobson, J. F.; Dinte, B. P. Constraint Satisfaction in Local and Gradient Susceptibility Approximations: Application to a van Der Waals Density Functional. *Phys. Rev. Lett.* **1996**, *76* (11), 1780.
- (51) Dion, M.; Rydberg, H.; Schröder, E.; Langreth, D. C.; Lundqvist, B. I. Van Der Waals Density Functional for General Geometries. *Phys. Rev. Lett.* **2004**, *92* (24), 246401.
- (52) Vydrov, O. A.; Van Voorhis, T. Nonlocal van Der Waals Density Functional Made Simple. *Phys. Rev. Lett.* **2009**, *103* (6), 063004.
- (53) Langreth, D.; Lundqvist, B. I.; Chakarova-Käck, S. D.; Cooper, V.; Dion, M.; Hyldgaard, P.; Kelkkanen, A.; Kleis, J.; Kong, L.; Li, S. A Density Functional for Sparse Matter. *J. Phys. Condens. Matter* **2009**, *21* (8), 084203.
- (54) Lee, K.; Murray, É. D.; Kong, L.; Lundqvist, B. I.; Langreth, D. C. Higher-Accuracy van Der Waals Density Functional. *Phys. Rev. B* **2010**, *82* (8), 081101.
- (55) Vydrov, O. A.; Van Voorhis, T. Nonlocal van Der Waals Density Functional: The Simpler the Better. *J. Chem. Phys.* **2010**, *133* (24), 244103.
- (56) Sabatini, R.; Gorni, T.; De Gironcoli, S. Nonlocal van Der Waals Density Functional Made Simple and Efficient. *Phys. Rev. B* **2013**, *87* (4), 041108.
- (57) Chakraborty, D.; Berland, K.; Thonhauser, T. Next-Generation Nonlocal van Der Waals Density Functional. *J. Chem. Theory Comput.* **2020**, *16* (9), 5893–5911.
- (58) Lin, I.-C.; Coutinho-Neto, M. D.; Felsenheimer, C.; von Lilienfeld, O. A.; Tavernelli, I.; Rothlisberger, U. Library of Dispersion-Corrected Atom-Centered Potentials for Generalized Gradient Approximation Functionals: Elements H, C, N, O, He, Ne, Ar, and Kr. *Phys. Rev. B* **2007**, *75* (20), 205131.
- (59) Mackie, I. D.; DiLabio, G. A. Interactions in Large, Polyaromatic Hydrocarbon Dimers: Application of Density Functional Theory with Dispersion Corrections. *J. Phys. Chem. A* **2008**, *112* (43), 10968–10976.
- (60) DiLabio, G. A. Accurate Treatment of van Der Waals Interactions Using Standard Density Functional Theory Methods with Effective Core-Type Potentials: Application to Carbon-Containing Dimers. *Chem. Phys. Lett.* **2008**, *455* (4–6), 348–353.
- (61) Torres, E.; DiLabio, G. A. A (Nearly) Universally Applicable Method for Modeling Noncovalent Interactions Using B3LYP. *J. Phys. Chem. Lett.* **2012**, *3* (13), 1738–1744.
- (62) Zhao, Y.; Schultz, N. E.; Truhlar, D. G. Exchange–Correlation Functional with Broad Accuracy for Metallic and Nonmetallic Compounds, Kinetics, and Noncovalent Interactions. *J. Chem. Phys.* **2005**, *123* (16), 161103.
- (63) Zhao, Y.; Truhlar, D. G. The M06 Suite of Density Functionals for Main Group Thermochemistry, Thermochemical Kinetics, Noncovalent Interactions, Excited States, and Transition Elements: Two New Functionals and Systematic Testing of Four M06-Class Functionals and 12 Other Functionals. *Theor. Chem. Acc.* **2008**, *120* (1), 215–241.
- (64) Peverati, R.; Truhlar, D. G. Exchange–Correlation Functional with Good Accuracy for Both Structural and Energetic Properties While Depending Only on the Density and Its Gradient. *J. Chem. Theory Comput.* **2012**, *8* (7), 2310–2319.
- (65) Perdew, J. P.; Kurth, S.; Zupan, A.; Blaha, P. Accurate Density Functional with Correct Formal Properties: A Step beyond the Generalized Gradient Approximation. *Phys. Rev. Lett.* **1999**, *82* (12), 2544.
- (66) Sun, J.; Ruzsinszky, A.; Perdew, J. P. Strongly Constrained and Appropriately Normed Semilocal Density Functional. *Phys. Rev. Lett.* **2015**, *115* (3), 036402.

- (67) Ohkubo, T.; Takei, A.; Tachi, Y.; Fukatsu, Y.; Deguchi, K.; Ohki, S.; Shimizu, T. New Approach To Understanding the Experimental  $^{133}\text{Cs}$  NMR Chemical Shift of Clay Minerals via Machine Learning and DFT-GIPAW Calculations. *J. Phys. Chem. A* **2023**, *127* (4), 973–986.
- (68) Giannozzi, P.; Baroni, S.; Bonini, N.; Calandra, M.; Car, R.; Cavazzoni, C.; Ceresoli, D.; Chiarotti, G. L.; Cococcioni, M.; Dabo, I. QUANTUM ESPRESSO: A Modular and Open-Source Software Project for Quantum Simulations of Materials. *J. Phys. Condens. Matter* **2009**, *21* (39), 395502.
- (69) Giannozzi, P.; Andreussi, O.; Brumme, T.; Bunau, O.; Nardelli, M. B.; Calandra, M.; Car, R.; Cavazzoni, C.; Ceresoli, D.; Cococcioni, M. Advanced Capabilities for Materials Modelling with Quantum ESPRESSO. *J. Phys. Condens. Matter* **2017**, *29* (46), 465901.
- (70) Dal Corso, A. Pseudopotentials Periodic Table: From H to Pu. *Comput. Mater. Sci.* **2014**, *95*, 337–350.
- (71) Hammer, B.; Hansen, L. B.; Nørskov, J. K. Improved Adsorption Energetics within Density-Functional Theory Using Revised Perdew-Burke-Ernzerhof Functionals. *Phys. Rev. B* **1999**, *59* (11), 7413.
- (72) Zhang, Y.; Yang, W. Comment on “Generalized Gradient Approximation Made Simple.” *Phys. Rev. Lett.* **1998**, *80* (4), 890.
- (73) Holmes, S. T.; Alkan, F.; Iuliucci, R. J.; Mueller, K. T.; Dybowski, C. Analysis of the Bond-valence Method for Calculating  $^{29}\text{Si}$  and  $^{31}\text{P}$  Magnetic Shielding in Covalent Network Solids. *J. Comput. Chem.* **2016**, *37* (18), 1704–1710.
- (74) Holmes, S. T.; Bai, S.; Iuliucci, R. J.; Mueller, K. T.; Dybowski, C. Calculations of Solid-state  $^{43}\text{Ca}$  NMR Parameters: A Comparison of Periodic and Cluster Approaches and an Evaluation of DFT Functionals. *J. Comput. Chem.* **2017**, *38* (13), 949–956.
- (75) Perdew, J. P.; Ruzsinszky, A.; Csonka, G. I.; Vydrov, O. A.; Scuseria, G. E.; Constantin, L. A.; Zhou, X.; Burke, K. Restoring the Density-Gradient Expansion for Exchange in Solids and Surfaces. *Phys. Rev. Lett.* **2008**, *100* (13), 136406.
- (76) Becke, A. D. On the Large-gradient Behavior of the Density Functional Exchange Energy. *J. Chem. Phys.* **1986**, *85* (12), 7184–7187. <https://doi.org/10.1063/1.451353>.
- (77) Becke, A. D.; Johnson, E. R. Exchange-Hole Dipole Moment and the Dispersion Interaction Revisited. *J. Chem. Phys.* **2007**, *127* (15).
- (78) Tao, J.; Zheng, F.; Gebhardt, J.; Perdew, J. P.; Rappe, A. M. Screened van Der Waals Correction to Density Functional Theory for Solids. *Phys. Rev. Mater.* **2017**, *1* (2), 020802.
- (79) Berland, K.; Chakraborty, D.; Thonhauser, T. Van Der Waals Density Functional with Corrected C 6 Coefficients. *Phys. Rev. B* **2019**, *99* (19), 195418.
- (80) Hamada, I. Van Der Waals Density Functional Made Accurate. *Phys. Rev. B* **2014**, *89* (12), 121103.
- (81) Holmes, S. T.; Schurko, R. W. Refining Crystal Structures with Quadrupolar NMR and Dispersion-Corrected Density Functional Theory. *J. Phys. Chem. C* **2018**, *122* (3), 1809–1820.
- (82) Yang, J. H.; Kitchaev, D. A.; Ceder, G. Rationalizing Accurate Structure Prediction in the Meta-GGA SCAN Functional. *Phys. Rev. B* **2019**, *100* (3), 035132.
- (83) Anatole von Lilienfeld, O.; Tkatchenko, A. Two- and Three-Body Interatomic Dispersion Energy Contributions to Binding in Molecules and Solids. *J. Chem. Phys.* **2010**, *132* (23).
- (84) Pyper, N. The Cohesive Energetics of Solid Cesium Chloride. *J. Chem. Phys.* **2003**, *118* (5), 2308–2324.
- (85) Aguado, A. Comment on “The Cohesive Energetics of Solid Cesium Chloride” [J. Chem. Phys. *118*, 2308 (2003)]. *J. Chem. Phys.* **2003**, *119* (16), 8765–8766.
- (86) Otero-de-la-Roza, A.; Johnson, E. R. Application of XDM to Ionic Solids: The Importance of Dispersion for Bulk Moduli and Crystal Geometries. *J. Chem. Phys.* **2020**, *153* (5), 054121.
- (87) Czernek, J.; Brus, J. Describing the Anisotropic  $^{133}\text{Cs}$  Solid State NMR Interactions in Cesium Chromate. *Chem. Phys. Lett.* **2017**, *684*, 8–13.
- (88) Halliday, J.; Hill, H.; Richards, R. Solvent Isotope Shifts of Caesium Resonances in Dilute Salt Solutions. *J. Chem. Soc. Chem. Commun.* **1969**, No. 5, 219–220.

- (89) Haase, A.; Kerber, M.; Kessler, D.; Kronenbitter, J.; Krüger, H.; Lutz, O.; Müller, M.; Nolle, A. Nuclear Magnetic Shielding and Quadrupole Coupling of  $^{133}\text{Cs}$  in Cesium Salt Powders. *Z. Für Naturforschung A* **1977**, *32* (9), 952–956.
- (90) Mooibroek, S.; Wasylishen, R. E.; Dickson, R.; Facey, G.; Pettitt, B. A. Simultaneous Observation of Shielding Anisotropies and Quadrupolar Splittings in Solid State  $^{133}\text{Cs}$  NMR Spectra. *J. Magn. Reson.* **1969** **1986**, *66* (3), 542–545.
- (91) Kolganov, A. A.; Gabrienko, A. A.; Chernyshov, I. Y.; Stepanov, A. G.; Pidko, E. A. The Accuracy Challenge of the DFT-Based Molecular Assignment of  $^{13}\text{C}$  MAS NMR Characterization of Surface Intermediates in Zeolite Catalysis. *Phys. Chem. Chem. Phys.* **2020**, *22* (41), 24004–24013.
- (92) Dietrich, B.; Lehn, J.; Sauvage, J. Les Cryptates. *Tetrahedron Lett.* **1969**, *10* (34), 2889–2892.
- (93) Wong, A.; Sham, S.; Wang, S.; Wu, G. A Solid-State  $^{133}\text{Cs}$  Nuclear Magnetic Resonance and X-Ray Crystallographic Study of Cesium Complexes with Macrocyclic Ligands. *Can. J. Chem.* **2000**, *78* (7), 975–985.
- (94) Tran, F.; Kalantari, L.; Traoré, B.; Rocquefelte, X.; Blaha, P. Nonlocal van Der Waals Functionals for Solids: Choosing an Appropriate One. *Phys. Rev. Mater.* **2019**, *3* (6), 063602.
- (95) Del Grande, R. R.; Menezes, M. G.; Capaz, R. B. Layer Breathing and Shear Modes in Multilayer Graphene: A DFT-vdW Study. *J. Phys. Condens. Matter* **2019**, *31* (29), 295301.
- (96) Takano, Y.; Kobayashi, N.; Morikawa, Y. Computational Study on Atomic Structures, Electronic Properties, and Chemical Reactions at Surfaces and Interfaces and in Biomaterials. *J. Phys. Soc. Jpn.* **2018**, *87* (6), 061013.
- (97) Abidin, A. F. Z.; Hamada, I. Interaction of Water with Nitrogen-Doped Graphene. *Phys. Rev. B* **2022**, *105* (7), 075416.
- (98) Bernasconi, D.; Bordignon, S.; Rossi, F.; Priola, E.; Nervi, C.; Gobetto, R.; Voinovich, D.; Hasa, D.; Duong, N. T.; Nishiyama, Y. Selective Synthesis of a Salt and a Cocrystal of the Ethionamide–Salicylic Acid System. *Cryst. Growth Des.* **2019**, *20* (2), 906–915.

## Supplementary Information:

### Prediction of NMR Parameters and geometry in $^{133}\text{Cs}$ -containing compounds using Density Functional Theory

N. Manukovsky<sup>1</sup>, N. Vaisleib<sup>1</sup>, M. Arbel-Haddad<sup>2</sup>, A. Goldbourt<sup>1</sup>

<sup>1</sup>School of Chemistry, Tel Aviv University, Ramat Aviv 6997801, Tel Aviv, Israel

<sup>2</sup>Nuclear Research Center Negev, PO Box 9001, Beer Sheva 84901, Israel

#### Computational parameters

Table S 1 lists the energy cutoff values and Monkhorst-Pack grid dimensions used in each calculation.

*Table S 1: energy cutoff and grid sizes used for the calculations.*

system	Ecut [Ry]	kgrid xyz
CsF	100	12 12 12
CsCl	80	8 8 8
CsBr	100	8 8 8
CsI	100	8 8 8
Cs <sub>2</sub> CrO <sub>4</sub>	80	5 6 4
CsClO <sub>4</sub>	100	7 6 4
Cs <sub>2</sub> SO <sub>4</sub>	100	8 6 5
CsVO <sub>3</sub>	110	10 7 10
CsGeCl <sub>3</sub>	100	12 12 12
CsGeBr <sub>3</sub>	100	12 12 12
CsGeI <sub>3</sub>	100	12 12 12
[Cs <sup>+</sup> (Cryptand[2.2.2])]I <sup>-</sup>	90	3 3 3

## Crystal structures and unit cell volumes

Table S 2 specifies the experimental and computational unit cell volumes, as well as the references for the crystal structures used as input for the structural optimizations.

Table S 2: Experimental and calculated unit cell volumes [ $\text{\AA}^3$ ] of the tested materials

	Exp	ref	PBE	rVV10	vdW-DF3- opt1	vdW-DF- C6	rev-vdW- DF2	PBE+ XDM	PBE+ D3
<b>CsF</b>	54.22	1	57.11	53.52	52.02	53.56	54.12	41.56	56.28
<b>CsCl</b>	70.09	2	74.24	68.54	66.25	68.22	68.92	50.97	74.36
<b>CsBr</b>	78.73	2	83.87	78.02	78.24	78.75	78.68	57.86	84.48
<b>CsI</b>	95.24	2	101.49	93.22	90.17	92.81	93.87	68.7 2	102.04
<b>Cs<sub>2</sub>CrO<sub>4</sub></b>	594.61	3	630.09	587.09	572.47	585.99	591.49	492.05	620.04
<b>CsClO<sub>4</sub></b>	458.28	4	499.01	447.12	438.86	449.31	455.34	401.77	480.19
<b>Cs<sub>2</sub>SO<sub>4</sub></b>	563.72	5	602.80	559.22	544.48	556.51	561.45	475.88	592.37
<b>CsVO<sub>3</sub></b>	382.21	6	418.31	381.22	371.36	380.15	384.94	356.19	408.41
<b>CsGeCl<sub>3</sub></b>	161.43	7	169.12	152.18	145.96	150.68	152.20	133.52	163.34
<b>CsGeBr<sub>3</sub></b>	179.98	7	189.43	174.38	165.74	170.85	173.06	153.34	181.75
<b>CsGeI<sub>3</sub></b>	215.37	7	228.01	214.47	203.09	208.46	211.53	184.93	219.52
<b>Cs<sup>+</sup>(Cryptand[2.2.2])<sup>-</sup></b>	1235	8	1438	1175		1184	1209		1234

	PBE + D2 Zhang	rPBE+ D2 Zhang	rPBE+ D2* Zhang	rPBE+ D2* Zhang	revPBE+ D3	PBEsol+ D2 Zhang	PBEsol+ D3	B86bPBE+ XDM
<b>CsF</b>	51.87	56.55	36.03	55.24	61.19	48.10	51.99	47.30
<b>CsCl</b>	67.51	72.80	48.64	72.80	79.42	63.21	67.32	58.74
<b>CsBr</b>	75.92	78.73	55.50	81.50	90.59	70.99	75.97	66.37
<b>CsI</b>	89.09	95.27	68.18	95.27	111.48	83.86	90.65	79.61
<b>Cs<sub>2</sub>CrO<sub>4</sub></b>	574.66	618.24	463.99	616.76	658.95	536.45	573.54	546.63
<b>CsClO<sub>4</sub></b>	455.49	497.34	417.34	497.02	499.35	425.70	450.57	429.84
<b>Cs<sub>2</sub>SO<sub>4</sub></b>	555.57	594.91	444.64	586.52	625.40	522.00	549.93	475.88
<b>CsVO<sub>3</sub></b>	374.63	409.59	335.44	408.01	427.01	349.24	375.67	354.54
<b>CsGeCl<sub>3</sub></b>	147.76	171.30	145.74	171.76	167.85	134.47	146.70	140.68
<b>CsGeBr<sub>3</sub></b>	165.04	185.94	160.81	186.76	185.40	153.50	164.10	159.23
<b>CsGeI<sub>3</sub></b>	199.25	218.47	193.80	216.10	227.74	185.48	200.71	194.96
<b>Cs<sup>+</sup>(Cryptand[2.2.2])<sup>-</sup></b>					1215		1144	

## Additional error metrics

Figure S 1 shows additional statistical parameters of the DFT calculations.

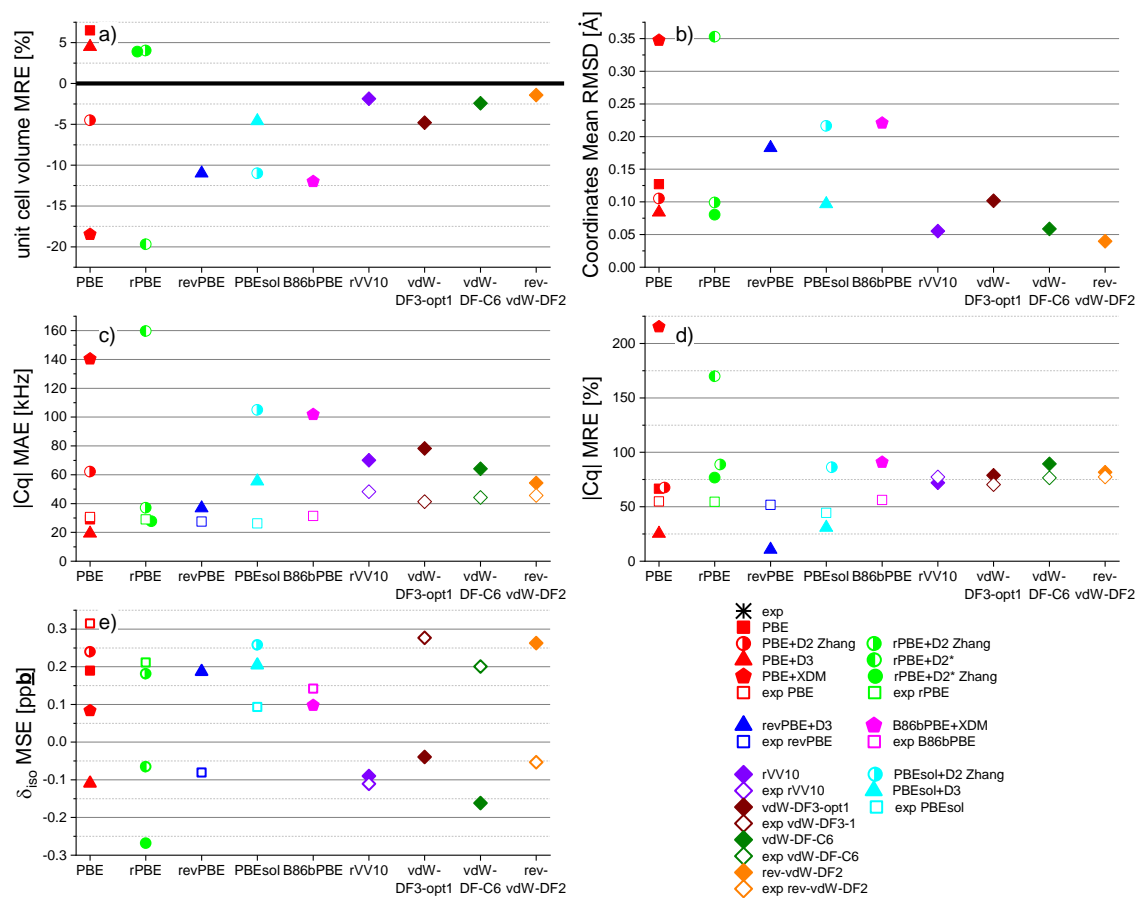


Figure S 1: Error metrics of DFT functionals: a) Mean Relative Error of the unit cell volume; b) Mean RMSD of the atom coordinates; c) Mean Absolute Error and d) Mean Relative Error of the quadrupolar coupling constant; e) Mean (Signed) Error of the isotropic chemical shift, in ppb.

## Quadrupolar coupling constants

Table S 3 – Table S 6 specify the experimental and computational quadrupolar coupling parameters of the tested materials.

Table S 3: Experimental quadrupolar coupling constants of the tested materials

	Experimental		
	Cq [kHz]	$\eta$	ref
<b>CsF</b>	0	0	
<b>CsCl</b>	0	0	
<b>CsBr</b>	0	0	
<b>CsI</b>	0	0	
<b>Cs<sub>2</sub>CrO<sub>4</sub> I</b>	365	0.56	<sup>9</sup>
	376	0.52	<sup>10</sup>
	373	0.55	<sup>11</sup>
<b>Cs<sub>2</sub>CrO<sub>4</sub> II</b>	142	0.11	<sup>9</sup>
	138	0.15	<sup>10</sup>
	142	0.15	<sup>11</sup>
<b>CsClO<sub>4</sub></b>	133.6	0.11	<sup>9</sup>
<b>Cs<sub>2</sub>SO<sub>4</sub> I</b>	20	0.27	<sup>9</sup>
<b>Cs<sub>2</sub>SO<sub>4</sub> II</b>	261	0.01	<sup>9</sup>
<b>CsVO<sub>3</sub></b>	225	0.47	<sup>9</sup>
<b>CsGeCl<sub>3</sub></b>	12	<0.10	<sup>7</sup>
<b>CsGeBr<sub>3</sub></b>	52	0	<sup>7</sup>
	50	0	
<b>CsGeI<sub>3</sub></b>	55	0.05	<sup>7</sup>
	52	0.05	
<b>Cs<sup>+</sup>(Cryptand[2.2.2])I<sup>-</sup></b>	1047	0.73	<sup>8</sup>

Table S 4: Calculated quadrupolar coupling constants – PBE and rPBE functionals

	PBE		Exp PBE		PBE + D2 Zhang		PBE+D3		PBE+XDM		rPBE + D2 Zhang		rPBE +D2*		rPBE +D2* Zhang		exp rPBE	
	Cq [kHz]	$\eta$	Cq [kHz]	$\eta$	Cq [kHz]	$\eta$	Cq [kHz]	$\eta$	Cq [kHz]	$\eta$	Cq [kHz]	$\eta$	Cq [kHz]	$\eta$	Cq [kHz]	$\eta$	Cq [kHz]	$\eta$
Cs <sub>2</sub> CrO <sub>4</sub> I	391	0.6	456	0.6	487	0.4	396	0.6	725	0.4	373	0.6	544	0.8	393	0.6	445	0.5
Cs <sub>2</sub> CrO <sub>4</sub> II	-136	0.5	-152	0.2	-183	0.4	-142	0.0	-193	0.1	-154	0.3	-450	0.0	-141	0.3	-153	0.3
CsClO <sub>4</sub>	156	0.3	194	0.8	304	0.1	203	0.2	430	0.2	218	0.3	406	0.1	155	0.3	189	0.8
Cs <sub>2</sub> SO <sub>4</sub> I	278	0.3	289	0.0	293	0.2	269	0.1	359	0.2	275	0.2	342	0.2	274	0.3	281	0.0
Cs <sub>2</sub> SO <sub>4</sub> II	82	0.3	64	0.6	116	0.5	43	0.1	242	0.2	79	0.5	212	0.6	84	0.3	62	0.7
CsVO <sub>3</sub>	140	0.2	238	0.3	266	0.3	195	0.8	373	0.8	146	0.5	571	1.0	159	0.5	244	0.1
CsGeCl <sub>3</sub>	41	0.0	28	0.0	11	0.0	20	0.0	53	0.0	56	0.0	8	0.0	48	0.0	29	0.0
CsGeBr <sub>3</sub>	60	0.0	56	0.0	20	0.0	43	0.0	17	0.0	73	0.0	17	0.0	64	0.0	57	0.0
CsGeI <sub>3</sub>	66	0.0	66	0.0	25	0.0	54	0.0	70	0.0	69	0.0	29	0.0	67	0.0	68	0.0
Cs <sup>+</sup> (Cryptand[2.2.2])I <sup>-</sup>	959	0.7					982.4	0.9										

Table S 5: Calculated quadrupolar coupling constants – additional semilocal functionals

	revPBE + D3		exp revPBE		PBEsol + D2 Zhang		PBEsol + D3		exp PBEsol		B86bPBE + XDM		exp B86bPBE	
	Cq [kHz]	$\eta$	Cq [kHz]	$\eta$	Cq [kHz]	$\eta$	Cq [kHz]	$\eta$	Cq [kHz]	$\eta$	Cq [kHz]	$\eta$	Cq [kHz]	$\eta$
Cs <sub>2</sub> CrO <sub>4</sub> I	276	0.8	444	0.5	616	0.3	506	0.6	451	0.6	573	0.6	458	0.6
Cs <sub>2</sub> CrO <sub>4</sub> II	-136	0.6	-153	0.3	-184	0.4	-155	0.0	-150	0.1	-169	0.1	-153	0.2
CsClO <sub>4</sub>	223	0.1	189	0.8	366	0.0	242	0.3	189	0.7	326	0.3	195	0.8
Cs <sub>2</sub> SO <sub>4</sub> I	258	0.0	282	0.0	327	0.1	290	0.0	291	0.0	323	0.2	290	0.0
Cs <sub>2</sub> SO <sub>4</sub> II	30	0.3	62	0.7	148	0.3	75	0.5	58	0.7	157	0.2	66	0.6
CsVO <sub>3</sub>	116	0.8	237	0.2	350	0.2	310	0.8	221	0.5	425	0.4	239	0.3
CsGeCl <sub>3</sub>	20	0.0	27	0.0	3	0.0	3	0.0	25	0.0	3	0.0	28	0.0
CsGeBr <sub>3</sub>	41	0.0	55	0.0	3	0.0	15	0.0	50	0.0	0	0.0	56	0.0
CsGeI <sub>3</sub>	57	0.0	65	0.0	6	0.0	28	0.0	59	0.0	18	0.0	66	0.0
Cs <sup>+</sup> (Cryptand[2.2.2])I <sup>-</sup>	952.1	0.9					1019.5	0.9						



Table S 6: Calculated quadrupolar coupling constants – nonlocal functionals

	rVV10		exp rVV10		vdW-DF3-opt1		exp vdW-DF3-opt1		vdW-DF-C6		exp vdW-DF-C6		rev-vdW-DF2		exp rev-vdW-DF2	
	Cq [kHz]	$\eta$	Cq [kHz]	$\eta$	Cq [kHz]	$\eta$	Cq [kHz]	$\eta$	Cq [kHz]	$\eta$	Cq [kHz]	$\eta$	Cq [kHz]	$\eta$	Cq [kHz]	$\eta$
<b>Cs<sub>2</sub>CrO<sub>4</sub> I</b>	529	0.6	500	0.6	539	0.6	479	0.6	511	0.6	488	0.6	496	0.6	486	0.6
<b>Cs<sub>2</sub>CrO<sub>4</sub> II</b>	-158	0.2	-154	0.3	-158	0.3	-153	0.3	-155	0.3	-154	0.3	-152	0.3	-154	0.3
<b>CsClO<sub>4</sub></b>	300	0.2	218	0.7	310	0.3	210	0.8	289	0.2	194	0.8	259	0.3	214	0.8
<b>Cs<sub>2</sub>SO<sub>4</sub> I</b>	319	0.2	309	0.1	322	0.2	301	0.1	315	0.2	303	0.1	310	0.2	302	0.1
<b>Cs<sub>2</sub>SO<sub>4</sub> II</b>	104	0.4	82	0.5	120	0.5	76	0.6	105	0.5	80	0.6	99	0.5	80	0.6
<b>CsVO<sub>3</sub></b>	354	0.5	272	0.2	358	0.5	257	0.3	323	0.5	270	0.2	296	0.4	268	0.2
<b>CsGeCl<sub>3</sub></b>	8	0.0	31	0.0	12	0.0	31	0.0	28	0.0	33	0.0	28	0.0	33	0.0
<b>CsGeBr<sub>3</sub></b>	37	0.0	63	0.0	27	0.0	61	0.0	41	0.0	65	0.0	44	0.0	65	0.0
<b>CsGeI<sub>3</sub></b>	54	0.0	73	0.0	29	0.0	72	0.0	58	0.0	77	0.0	61	0.0	77	0.0
<b>Cs<sup>+</sup>(Cryptand[2.2.2])I<sup>-</sup></b>	1068.5	0.9							1072.4	0.9			1070.7	0.9		

## Scaling the quadrupolar coupling constants

Figure S 2 and Table S 7 show a fairly linear, though noisy, correlation between the computational  $|Cq|$  obtained by various functionals (shown are the best performing functionals in terms of  $Cq$ ). Similar trends were reported for  $^{133}\text{Cs}^{12}$  and for several other half-integer quadrupolar nuclei<sup>13</sup>.

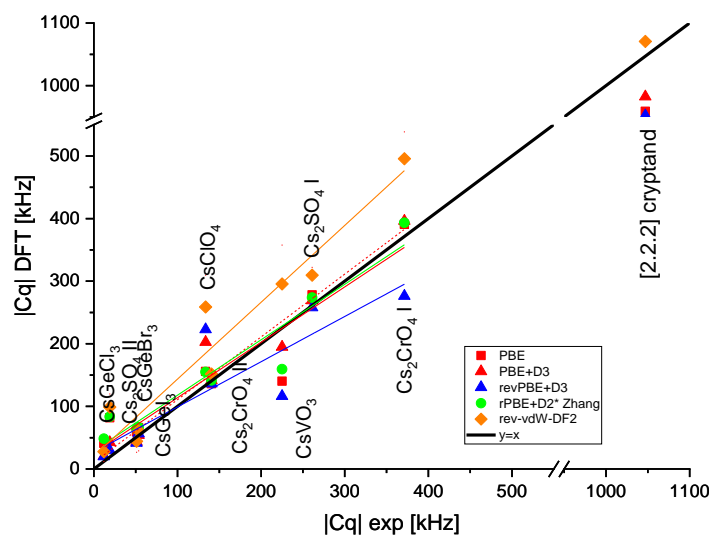


Figure S 2: Calculated vs experimental quadrupolar coupling constants of selected functionals.

Table S 7: linear fit parameters for Figure S 2.

functional	Intercept $\pm$ SE [kHz]	Slope $\pm$ SE	R <sup>2</sup>
PBE	25 $\pm$ 21	0.89 $\pm$ 0.11	0.88
PBE+D3	10 $\pm$ 15	1.00 $\pm$ 0.08	0.95
revPBE+D3	27 $\pm$ 27	0.72 $\pm$ 0.15	0.74
rPBE+D2* Zhang	29 $\pm$ 18	0.89 $\pm$ 0.10	0.91
rev-vdW-DF2	21 $\pm$ 23	1.23 $\pm$ 0.13	0.92

## $^{87}\text{Rb}$ Quadrupolar coupling constants

The quadrupolar coupling constant of  $^{133}\text{Cs}$  is small due its low quadrupolar moment ( $-0.00343 \text{ b}^{14}$ ). This raised the question whether the differences between Cq values obtained by various functionals fall within the error range. To check this, we performed similar calculations using a nucleus with a much larger quadrupolar moment ( $0.1335 \text{ b}^{14}$ ) –  $^{87}\text{Rb}$ . The results (Figure S 3) show the same trend observed in  $^{133}\text{Cs}$  repeats itself in  $^{87}\text{Rb}$ . We therefore conclude that the differences between Cq of various functionals reflect inherent differences between these functionals.

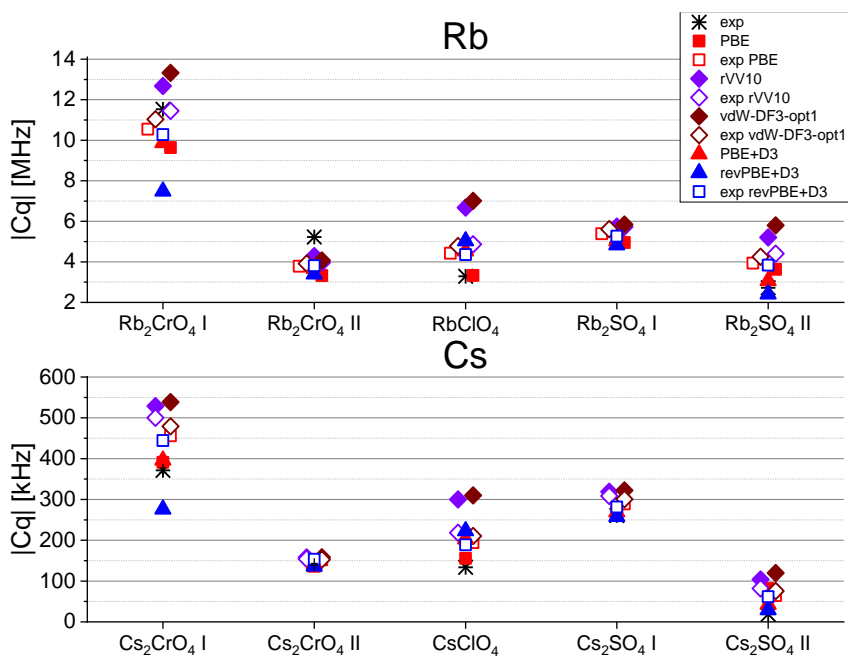


Figure S 3: Quadrupolar coupling constants of Rb salts, compared with Cs salts. The experimental  $^{87}\text{Rb}$  data are taken from previously reported studies<sup>15–17</sup>.

## Chemical Shifts

Table S 8 - Table S 12 specify the experimental and computational  $^{133}\text{Cs}$  chemical shift parameters of the materials discussed in the main text.

To generate consistent experimental values, we re-referenced the results of several studies to fit a uniform scale, where solid CsCl resonates at 223.2 ppm, as commonly used. Since some studies also used a 1M solution of CsCl as a reference<sup>18</sup> and some studies were performed at static conditions, we also acquired our own data at room temperature using a 14.1T magnet and 5 kHz spinning. We measured solid samples of CsCl, CsI,  $\text{Cs}_2\text{CrO}_4$ , and  $\text{Cs}_2\text{SO}_4$ . We also performed experiments on 5 solutions of CsCl at different concentrations at the range of 0.1-1 [M], and obtained a linear fit where  $\delta_{\text{iso}}(^{133}\text{Cs}, \text{ppm}) = 11.3 \pm 0.2[C] - 6.1 \pm 0.2$ . This result was obtained by referencing all data to solid CsCl at 223.2 ppm and is consistent with infinite dilution values reported by Haase<sup>19</sup> though with some deviations for his reported value of 0.5M CsCl. Our experimental results are shown in Figure S 4.

Table S 8: Experimental chemical shifts [ppm] of the materials examined in this work.

	Experimental			ref
	$\delta_{\text{iso}}$	$\Delta\delta = \delta_{\text{zz}} - (\delta_{\text{xx}} + \delta_{\text{yy}})/2$	$\eta = (\delta_{\text{yy}} - \delta_{\text{xx}})/(\delta_{\text{zz}} - \delta_{\text{iso}})$	
<b>CsF</b>	181.3*	0	0	18
<b>CsCl</b>	223.2	0	0	20
<b>CsBr</b>	256.0*	0	0	18
	258.2	0	0	20
<b>CsI</b>	276.1*	0	0	18
	275.7	0	0	This work
<b>Cs<sub>2</sub>CrO<sub>4</sub> I</b>	-98.3^	-328.5	0.04	11
	-98.3	-331.5	0.06	9
	-100	-333	0.04	10
	-97.9			This work
<b>Cs<sub>2</sub>CrO<sub>4</sub> II</b>	28.7^	246	0.3	11
	28.2	243	0.31	9
	27.0	244.5	0.26	10
	27.9			This work
<b>CsClO<sub>4</sub></b>	2.7	34.35	0.32	9
<b>Cs<sub>2</sub>SO<sub>4</sub> I</b>	68.6	-22.45	0.14	9
	68.2			This work
<b>Cs<sub>2</sub>SO<sub>4</sub> II</b>	100.3	-46.5	0.49	9
	100.1			This work
<b>CsVO<sub>3</sub></b>	-32.0	-135	0.44	9
<b>CsGeCl<sub>3</sub></b>	36.9	10	0	7
	33.7	10	0	
<b>CsGeBr<sub>3</sub></b>	48.2	-9	1	7
	47.5	16	0	
<b>CsGeI<sub>3</sub></b>	41.8	NA	NA	7
	39.2			
<b>Cs<sup>+</sup>(Cryptand[2.2.2])I<sup>-</sup></b>	225	39	0.92	21

\* Originally referenced to 1 M CsCl=0 ppm. Our measurements show that with respect to solid CsCl at 223.2 ppm, the shift is 5.0 ppm.

^ Originally reported values with respect to 0.5 m CsCl. If the value was taken as 6.1 ppm without measurement, all the values need to be increased by 6.1 ppm. If the solution was measured, values need to be increased by 6.7 ppm in agreement with our results of -0.6 ppm for 0.5M CsCl. The values for  $\text{Cs}_2\text{CrO}_4$  are therefore 28.1 and -98.9, or 28.7 and -98.3. The latter were used in our calculations.

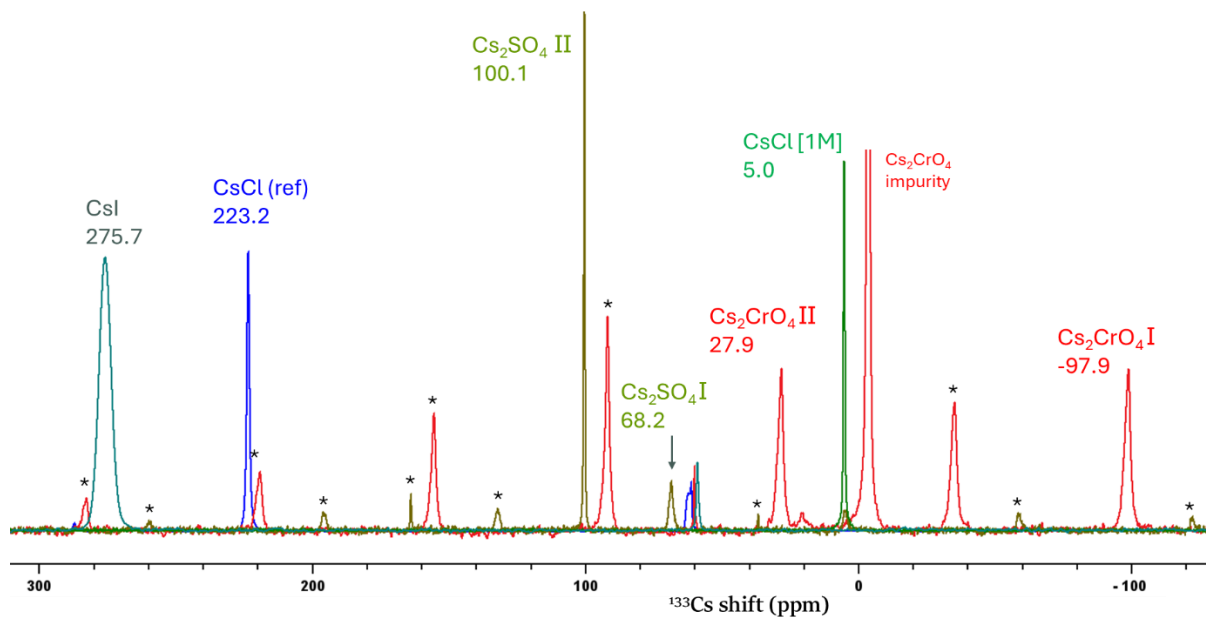


Figure S 4: Overlay of  $^{133}\text{Cs}$  5 kHz magic-angle spinning solid-state NMR spectra of Cs salts measured on a 14.1T magnet. All data were referenced to solid CsCl at 223.2 ppm. Powder samples were used as purchased and contain some minor contaminants. The  $\text{Cs}_2\text{CrO}_4$  sample has a large contaminant at  $\sim 0$  ppm but the two sites are clearly resolved. Spinning sidebands, marked by asterisk, were determined by collecting additional experiments at 6.66 and 7.50 kHz.

Table S 9: Calculated Chemical shifts [ppm] – PBE functionals

	PBE			Exp PBE			PBE + D2 Zhang			PBE+D3			PBE+XDM		
	$\delta_{\text{iso}}$	$\Delta\delta$	$\eta$	$\delta_{\text{iso}}$	$\Delta\delta$	$\eta$	$\delta_{\text{iso}}$	$\Delta\delta$	$\eta$	$\delta_{\text{iso}}$	$\Delta\delta$	$\eta$	$\delta_{\text{iso}}$	$\Delta\delta$	$\eta$
CsF	198.8	0	0	200.2	0	0	196.3	0	0	209.3	0	0	226.3	0	0
CsCl	230.7	0	0	226.5	0	0	216.4	0	0	226.3	0	0	241.6	0	0
CsBr	261.6	0	0	268.3	0	0	251.9	0	0	254.7	0	0	259.1	0	0
CsI	270.5	0	0	276.2	0	0	291.7	0	0	266.0	0	0	273.1	0	0
Cs <sub>2</sub> CrO <sub>4</sub> I	-69.4	-277.0	0.16	-69.5	-309.3	0.28	-85.7	-347.0	0.42	-84.7	-276.5	0.03	-41.2	-453.6	0.44
Cs <sub>2</sub> CrO <sub>4</sub> II	26.8	356.3	0.01	37.2	378.0	0.02	32.1	389.2	0.07	25.5	350.3	0.03	56.1	541.5	0.05
CsClO <sub>4</sub>	5.4	43.9	0.38	14.1	50.2	0.90	-0.3	63.1	0.19	15.5	52.9	0.25	7.8	81.1	0.56
Cs <sub>2</sub> SO <sub>4</sub> I	74.1	38.1	0.91	69.3	-47.0	0.16	57.3	-46.0	0.48	72.7	-38.5	0.79	59.7	-78.7	0.20
Cs <sub>2</sub> SO <sub>4</sub> II	103.8	19.8	0.62	102.5	17.2	0.16	90.2	-10.5	0.58	103.9	-11.3	0.50	96.5	-30.4	0.45
CsVO <sub>3</sub>	-34.7	-165.9	0.30	-13.6	-172.0	0.46	-19.6	-186.2	0.58	-36.1	-159.7	0.45	-29.1	-190.5	0.28
CsGeCl <sub>3</sub>	9.8	-19.9	0	-9.6	-16.9	0.00	26.6	-9.4	0.00	12.2	-12.5	0.00	3.2	-9.9	0.00
CsGeBr <sub>3</sub>	29.8	-24.8	0	13.7	-23.5	0.00	42.0	-11.0	0.00	38.4	-17.5	0.00	-16.5	-22.5	0.00
CsGeI <sub>3</sub>	18.9	-12.9	0	10.9	-14.9	0.00	27.2	-9.5	0.00	22.5	-9.5	0.00	-10.4	-22.2	0.00
Cs <sup>+</sup> (Cryptand[2.2.2]) <sup>-</sup>	254.3	-22.6	0.9							264.8	-9.7	0.33			

Table S 10: Calculated Chemical shifts [ppm] – rPBE functionals

	rPBE + D2 Zhang			rPBE +D2*			rPBE +D2* Zhang			exp rPBE		
	$\delta_{\text{iso}}$	$\Delta\delta$	$\eta$	$\delta_{\text{iso}}$	$\Delta\delta$	$\eta$	$\delta_{\text{iso}}$	$\Delta\delta$	$\eta$	$\delta_{\text{iso}}$	$\Delta\delta$	$\eta$
CsF	178.3	0.0	0.00	323.8	0.0	0.00	199.0	0.0	0.00	198.8	0.0	0.00
CsCl	210.6	0.0	0.00	234.3	0.0	0.00	210.0	0.0	0.00	221.0	0.0	0.00
CsBr	282.8	0.0	0.00	247.9	0.0	0.00	277.4	0.0	0.00	268.5	0.0	0.00
CsI	291.6	0.0	0.00	238.5	0.0	0.00	280.4	0.0	0.00	275.4	0.0	0.00
Cs <sub>2</sub> CrO <sub>4</sub> I	-60.0	-273.1	0.31	-21.8	-553.1	0.36	-58.8	-262.4	0.23	-80.6	-281.6	0.27
Cs <sub>2</sub> CrO <sub>4</sub> II	38.4	313.6	0.06	91.5	331.9	0.35	30.5	331.6	0.01	22.2	351.5	0.01
CsClO <sub>4</sub>	0.6	48.3	0.12	-29.5	71.2	0.40	-7.4	40.7	0.42	13.2	50.2	0.90
Cs <sub>2</sub> SO <sub>4</sub> I	69.2	33.8	0.89	88.1	-81.3	0.23	74.7	-37.2	0.81	78.8	-42.4	0.24
Cs <sub>2</sub> SO <sub>4</sub> II	93.4	8.4	0.88	99.8	-60.7	0.97	102.1	16.7	0.56	110.2	14.8	0.30
CsVO <sub>3</sub>	-20.6	-151.5	0.41	-13.4	209.1	0.99	-22.6	-152.6	0.34	2.1	-158.8	0.47
CsGeCl <sub>3</sub>	-11.0	-21.4	0.00	-49.8	-12.0	0.00	-14.4	-19.6	0.00	-10.6	-15.2	0.00
CsGeBr <sub>3</sub>	22.5	-25.3	0.00	-38.8	-13.6	0.00	18.8	-24.9	0.00	14.0	-22.8	0.00
CsGeI <sub>3</sub>	30.3	-10.0	0.00	-44.4	-17.5	0.00	36.5	-14.6	0.00	13.2	-15.7	0.00

Table S 11: Calculated Chemical shifts [ppm] – additional semilocal functionals

	revPBE + D3			exp revPBE			PBEsol + D2 Zhang			PBEsol + D3			exp PBEsol			B86bPBE + XDM			exp B86bPBE		
	$\delta_{\text{iso}}$	$\Delta\delta$	$\eta$	$\delta_{\text{iso}}$	$\Delta\delta$	$\eta$	$\delta_{\text{iso}}$	$\Delta\delta$	$\eta$	$\delta_{\text{iso}}$	$\Delta\delta$	$\eta$	$\delta_{\text{iso}}$	$\Delta\delta$	$\eta$	$\delta_{\text{iso}}$	$\Delta\delta$	$\eta$	$\delta_{\text{iso}}$	$\Delta\delta$	$\eta$
CsF	195.1	0.0	0.00	196.9	0.0	0.00	220.1	0.0	0.00	201.1	0.0	0.00	201.7	0.0	0.00	198.3	0.0	0.00	200.1	0.0	0.00
CsCl	235.9	0.0	0.00	230.6	0.0	0.00	217.3	0.0	0.00	223.9	0.0	0.00	238.5	0.0	0.00	238.0	0.0	0.00	224.9	0.0	0.00
CsBr	261.8	0.0	0.00	268.6	0.0	0.00	250.9	0.0	0.00	254.5	0.0	0.00	262.7	0.0	0.00	265.5	0.0	0.00	268.3	0.0	0.00
CsI	250.0	0.0	0.00	277.3	0.0	0.00	279.9	0.0	0.00	275.6	0.0	0.00	270.3	0.0	0.00	278.0	0.0	0.00	275.1	0.0	0.00
Cs <sub>2</sub> CrO <sub>4</sub> I	-101.7	-219.6	0.16	-69.5	-288.2	0.26	-88.6	-420.8	0.46	-85.9	-353.7	0.28	-66.0	-321.8	0.31	-69.1	-368.7	0.32	-80.0	-305.4	0.26
Cs <sub>2</sub> CrO <sub>4</sub> II	19.8	265.8	0.08	34.4	352.6	0.00	37.7	479.2	0.07	24.7	436.6	0.03	37.5	406.3	0.04	27.6	446.4	0.04	26.2	378.9	0.00
CsClO <sub>4</sub>	14.6	47.3	0.05	13.6	47.7	0.89	-1.8	73.4	0.48	0.9	62.6	0.50	8.6	51.5	0.99	8.9	72.9	0.43	26.3	50.2	0.90
Cs <sub>2</sub> SO <sub>4</sub> I	74.6	32.5	0.67	72.0	-43.0	0.23	52.2	-64.6	0.06	61.0	-54.2	0.11	71.4	-50.9	0.10	55.8	-78.7	0.20	73.1	-47.0	0.16
Cs <sub>2</sub> SO <sub>4</sub> II	101.1	-5.2	0.77	104.2	15.1	0.32	92.3	-13.3	0.85	97.0	-14.1	0.86	103.9	18.8	0.04	91.1	-30.4	0.45	106.2	17.2	0.16
CsVO <sub>3</sub>	-36.1	-128.1	0.52	-1.7	-158.5	0.46	-12.0	-214.8	0.70	-28.1	-195.4	0.59	-18.3	-183.9	0.50	-3.0	-189.1	0.65	-0.8	-168.9	0.44
CsGeCl <sub>3</sub>	21.4	-11.3	0.00	-12.0	-16.4	0.00	46.0	-8.5	0.00	33.4	-8.4	0.00	-5.6	-17.6	0.00	18.0	-5.8	0.00	-12.3	-16.0	0.00
CsGeBr <sub>3</sub>	61.6	-16.1	0.00	11.3	-23.2	0.00	6.3	-21.1	0.00	46.9	-13.0	0.00	15.5	-24.7	0.00	16.9	-10.9	0.00	15.0	-23.4	0.00
CsGeI <sub>3</sub>	28.1	-10.8	0.00	0.4	-14.5	0.00	25.8	-19.9	0.00	21.3	-11.1	0.00	6.1	-14.0	0.00	0.2	-12.7	0.00	4.1	-13.7	0.00
Cs <sup>+</sup> (Cryptand[2.2.2]) <sup>+</sup> I <sup>-</sup>	349.6	20.0	0.38							204.3	16.6	0.42									

Table S 12: Calculated Chemical shifts [ppm] – non-local functionals

	rVV10			exp rVV10			vdW-DF3-opt1			exp vdW-DF3-opt1			vdW-DF-C6			exp vdW-DF-C6			rev-vdW-DF2			exp rev-vdW-DF2		
	$\delta_{\text{iso}}$	$\Delta\delta$	$\eta$	$\delta_{\text{iso}}$	$\Delta\delta$	$\eta$	$\delta_{\text{iso}}$	$\Delta\delta$	$\eta$	$\delta_{\text{iso}}$	$\Delta\delta$	$\eta$	$\delta_{\text{iso}}$	$\Delta\delta$	$\eta$	$\delta_{\text{iso}}$	$\Delta\delta$	$\eta$	$\delta_{\text{iso}}$	$\Delta\delta$	$\eta$	$\delta_{\text{iso}}$	$\Delta\delta$	$\eta$
CsF	190.5	0.0	0.00	194.6	0.0	0.00	196.6	0.0	0.00	191.1	0.0	0.00	188.9	0.0	0.00	210.6	0.0	0.00	185.8	0.0	0.00	193.4	0.0	0.00
CsCl	223.6	0.0	0.00	227.4	0.0	0.00	240.0	0.0	0.00	226.2	0.0	0.00	233.1	0.0	0.00	242.8	0.0	0.00	231.4	0.0	0.00	223.9	0.0	0.00
CsBr	254.5	0.0	0.00	266.0	0.0	0.00	226.2	0.0	0.00	267.6	0.0	0.00	241.2	0.0	0.00	281.2	0.0	0.00	251.7	0.0	0.00	263.4	0.0	0.00
CsI	279.2	0.0	0.00	276.0	0.0	0.00	283.4	0.0	0.00	273.2	0.0	0.00	280.5	0.0	0.00	224.0	0.0	0.00	275.4	0.0	0.00	273.2	0.0	0.00
Cs <sub>2</sub> CrO <sub>4</sub> I	-99.4	-352.5	0.30	-74.1	-341.5	0.30	-101.8	-359.9	0.30	-83.8	-325.5	0.30	-100.4	-339.2	0.30	-84.5	-327.0	0.30	-95.7	-331.7	0.30	-86.9	-325.8	0.30
Cs <sub>2</sub> CrO <sub>4</sub> II	21.9	433.4	0.00	37.9	426.4	0.00	19.3	441.2	0.00	26.6	410.0	0.00	19.1	419.1	0.00	34.9	405.7	0.00	19.6	411.9	0.00	22.1	404.6	0.00
CsClO <sub>4</sub>	39.1	74.2	0.23	14.7	54.7	0.87	30.4	71.5	0.36	17.8	52.1	0.87	29.8	68.6	0.23	-0.2	50.2	0.90	25.9	64.4	0.29	26.4	53.0	0.84
Cs <sub>2</sub> SO <sub>4</sub> I	68.9	-51.2	0.38	64.3	-54.6	0.04	68.6	-54.8	0.21	77.4	-51.4	0.09	70.6	-51.0	0.28	83.6	-52.2	0.04	71.9	-49.4	0.32	74.1	-51.6	0.04
Cs <sub>2</sub> SO <sub>4</sub> II	107.3	-18.3	0.52	98.5	21.0	0.09	111.0	-18.0	0.87	112.0	19.8	0.09	110.0	-16.0	0.95	120.4	19.7	0.10	109.3	-15.3	1.00	107.8	19.6	0.07
CsVO <sub>3</sub>	-21.1	-189.9	0.51	-25.4	-192.5	0.45	-26.1	-193.6	0.58	-5.4	-179.1	0.43	-25.3	-183.8	0.51	-26.0	-181.7	0.47	-28.2	-181.8	0.51	-21.8	-182.5	0.49
CsGeCl <sub>3</sub>	28.0	-7.2	0.00	-2.5	-17.3	0.00	35.0	-9.5	0.00	-3.9	-17.5	0.00	30.0	-13.1	0.00	-3.3	-16.6	0.00	32.2	-13.2	0.00	6.2	-18.3	0.00
CsGeBr <sub>3</sub>	29.9	-11.9	0.00	27.3	-24.2	0.00	36.9	-12.7	0.00	18.3	-24.2	0.00	36.1	-12.4	0.00	26.1	-23.8	0.00	35.4	-14.0	0.00	26.7	-23.9	0.00
CsGeI <sub>3</sub>	3.8	-3.3	0.00	21.6	-11.8	0.00	6.6	-8.5	0.00	8.9	-12.9	0.00	12.4	-6.3	0.00	16.6	-12.4	0.00	11.5	-6.6	0.00	17.5	-12.5	0.00
Cs <sup>+</sup> (Cryptand[2.2.2]) <sup>+</sup> I <sup>-</sup>	198.7	30.4	0.04										223.6	22.7	0.09				228.7	19.1	0.11			

## Chemical Shift Anisotropy

Figure S 5 shows the chemical shift anisotropies of cesium oxyanions and perovskites. It can be seen that variations between functionals are substantial only for large CSA values. As only two such values were tested, no conclusion can be drawn about the relative accuracy of various functionals in this respect.

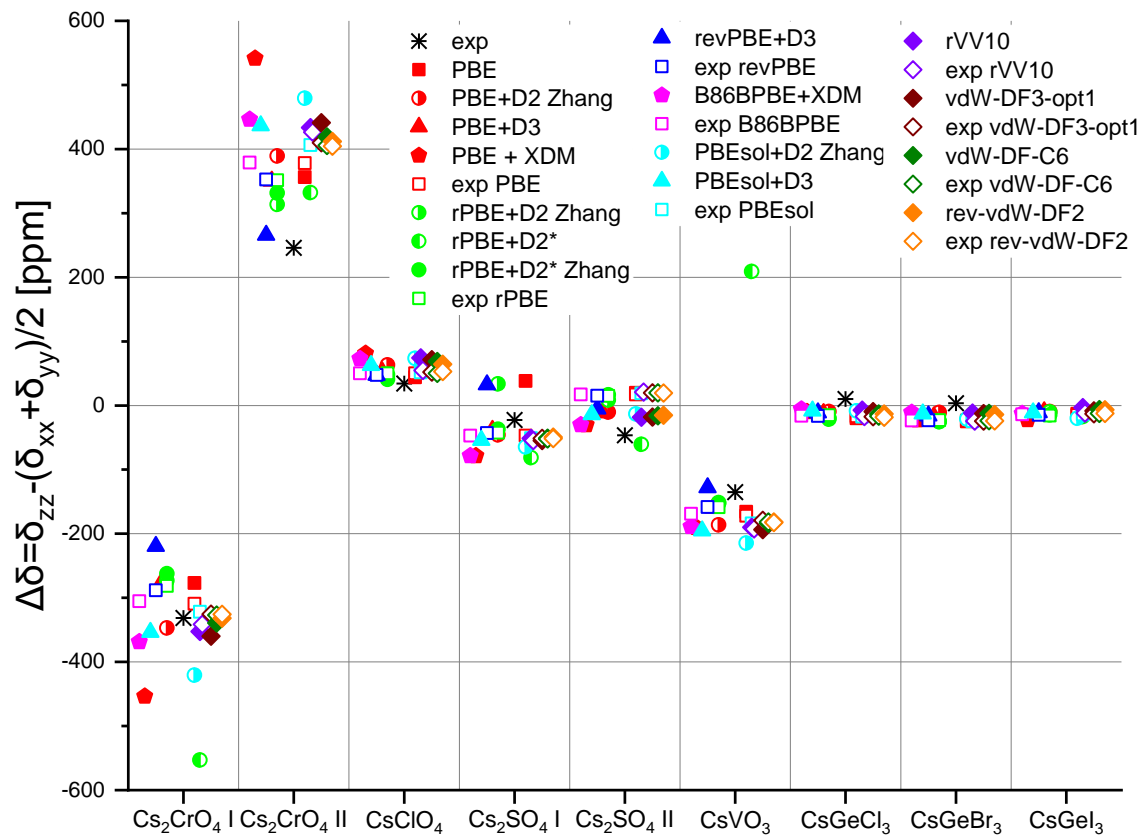


Figure S 5: Calculated vs experimental chemical shift anisotropies.



## Fully relativistic geometry optimization

The calculations in this work were run using scalar-relativistic pseudopotentials. In order to ascertain the validity of this approach, we carried out one geometry optimization using fully relativistic pseudopotentials. Then, the NMR parameters were calculated using scalar-relativistic PPs, as GIPAW currently does not support non-collinear calculations. The functional used was PBE. The results (Table S 13) show that the use of the scalar-relativistic approximation is justified.

Table S 13: results of scalar-relativistic vs fully relativistic calculations on  $\text{Cs}_2\text{CrO}_4$ .

	Unit cell volume [ $\text{\AA}^3$ ]			Optimization wall time on 32 cores [d]		Cq  [kHz]			$\delta_{\text{iso}}$ [ppm]		
	exp	Scalar relativistic	Fully relativistic	Scalar relativistic	Fully relativistic	exp	Scalar relativistic	Fully relativistic	exp	Scalar relativistic	Fully relativistic
site I	594.61	630.10	634.70	3.5	8.5	365 <sup>9</sup>	390.8	388.6	-98.3 <sup>11</sup>	-69.4	-64.2
						376 <sup>10</sup>					
site II						142 <sup>9</sup>	-136.1	-130.1	28.7 <sup>11</sup>	26.8	27.4
					138 <sup>10</sup>				28.2 <sup>9</sup>		
					142 <sup>11</sup>				27.0 <sup>10</sup>		

## References

- (1) Davey, W. P. Precision Measurements of Crystals of the Alkali Halides. *Phys. Rev.* **1923**, *21* (2), 143.
- (2) Wyckoff, R. W. *Crystal Structures*, 2nd ed.; Interscience: New York, 1963; Vol. 5.
- (3) Morris, A.; Kennard, C.; Moore, F.; Smith, G.; Berendsen, H. J. C. Cesium Chromate, CrCs<sub>2</sub>O<sub>4</sub> (Neutron). *Cryst. Struct. Commun.* **1981**, *10* (3), 529–532.
- (4) Granzin, J. Refinement of the Crystal Structures of RbClO<sub>4</sub> and CsClO<sub>4</sub>. *Z. Für Krist.-Cryst. Mater.* **1988**, *184* (1–4), 157–160.
- (5) Weber, H.; Schulz, M.; Schmitz, S.; Granzin, J.; Siegert, H. Determination and Structural Application of Anisotropic Bond Polarisabilities in Complex Crystals. *J. Phys. Condens. Matter* **1989**, *1* (44), 8543.
- (6) Hawthorne, F.; Calvo, C. The Crystal Chemistry of the M<sup>+</sup>VO<sub>3</sub> (M<sup>+</sup>= Li, Na, K, NH<sub>4</sub>, Tl, Rb, and Cs) Pyroxenes. *J. Solid State Chem.* **1977**, *22* (2), 157–170.
- (7) Hooper, R. W.; Ni, C.; Tkachuk, D. G.; He, Y.; Terskikh, V. V.; Veinot, J. G.; Michaelis, V. K. Exploring Structural Nuances in Germanium Halide Perovskites Using Solid-State <sup>73</sup>Ge and <sup>133</sup>Cs NMR Spectroscopy. *J. Phys. Chem. Lett.* **2022**, *13* (7), 1687–1696.
- (8) Moon, C. J.; Park, J.; Im, H.; Ryu, H.; Choi, M. Y.; Kim, T. H.; Kim, J. Chemical Shift and Second-Order Quadrupolar Effects in the Solid-State <sup>133</sup>Cs NMR Spectra of [Cs<sup>+</sup> (Cryptand [2.2. 2])] X (X= I<sup>-</sup>, SCN<sup>-</sup>, H<sub>2</sub>O). *Bull. Korean Chem. Soc.* **2020**, *41* (7), 702–708.
- (9) Skibsted, J.; Vosegaard, T.; Bildsøe, H.; Jakobsen, H. J. <sup>133</sup>Cs Chemical Shielding Anisotropies and Quadrupole Couplings from Magic-Angle Spinning NMR of Cesium Salts. *J. Phys. Chem.* **1996**, *100* (36), 14872–14881.
- (10) Power, W. P.; Mooibroek, S.; Wasylishen, R. E.; Cameron, T. S. Cesium-133 Single-Crystal NMR Study of Cesium Chromate. *J. Phys. Chem.* **1994**, *98* (6), 1552–1560.
- (11) Power, W. P.; Wasylishen, R. E.; Mooibroek, S.; Pettitt, B. A.; Danchura, W. Simulation of NMR Powder Line Shapes of Quadrupolar Nuclei with Half-Integer Spin at Low-Symmetry Sites. *J. Phys. Chem.* **1990**, *94* (2), 591–598.
- (12) Czernek, J.; Brus, J. Describing the Anisotropic <sup>133</sup>Cs Solid State NMR Interactions in Cesium Chromate. *Chem. Phys. Lett.* **2017**, *684*, 8–13.
- (13) Perras, F. A.; Bryce, D. L. Multinuclear Magnetic Resonance Crystallographic Structure Refinement and Cross-Validation Using Experimental and Computed Electric Field Gradients: Application to Na<sub>2</sub>Al<sub>2</sub>B<sub>2</sub>O<sub>7</sub>. *J. Phys. Chem. C* **2012**, *116* (36), 19472–19482.
- (14) Stone, N. Table of Nuclear Electric Quadrupole Moments. *At. Data Nucl. Data Tables* **2016**, *111*, 1–28.
- (15) Cheng, J. T.; Edwards, J. C.; Ellis, P. D. Measurement of Quadrupolar Coupling Constants, Shielding Tensor Elements and the Relative Orientation of Quadrupolar and Shielding Tensor Principal Axis Systems for Rubidium-87 and Rubidium-85 Nuclei in Rubidium Salts by Solid-State NMR. *J. Phys. Chem.* **1990**, *94* (2), 553–561.
- (16) Vosegaard, T.; Skibsted, J.; Bildsøe, H.; Jakobsen, H. J. Quadrupole Coupling and Anisotropic Shielding from Single-Crystal NMR of the Central Transition for Quadrupolar Nuclei. <sup>87</sup>Rb NMR of RbClO<sub>4</sub> and Rb<sub>2</sub>SO<sub>4</sub>. *J. Magn. Reson. A* **1996**, *122* (2), 111–119.
- (17) Vosegaard, T.; Skibsted, J.; Bildsøe, H.; Jakobsen, H. J. Combined Effect of Second-Order Quadrupole Coupling and Chemical Shielding Anisotropy on the Central Transition in MAS NMR of Quadrupolar Nuclei. <sup>87</sup>Rb MAS NMR of RbClO<sub>4</sub>. *J. Phys. Chem.* **1995**, *99* (27), 10731–10735.
- (18) Hayashi, S.; Hayamizu, K. Accurate Determination of NMR Chemical Shifts in Alkali Halides and Their Correlation with Structural Factors. *Bull. Chem. Soc. Jpn.* **1990**, *63* (3), 913–919.
- (19) Haase, A.; Kerber, M.; Kessler, D.; Kronenbitter, J.; Krüger, H.; Lutz, O.; Müller, M.; Nolle, A. Nuclear Magnetic Shielding and Quadrupole Coupling of <sup>133</sup>Cs in Cesium Salt Powders. *Z. Für Naturforschung A* **1977**, *32* (9), 952–956.
- (20) Mooibroek, S.; Wasylishen, R. E.; Dickson, R.; Facey, G.; Pettitt, B. A. Simultaneous Observation of Shielding Anisotropies and Quadrupolar Splittings in Solid State <sup>133</sup>Cs NMR Spectra. *J. Magn. Reson.* **1969** **1986**, *66* (3), 542–545.
- (21) Wong, A.; Sham, S.; Wang, S.; Wu, G. A Solid-State <sup>133</sup>Cs Nuclear Magnetic Resonance and X-Ray Crystallographic Study of Cesium Complexes with Macrocyclic Ligands. *Can. J. Chem.* **2000**, *78* (7), 975–985.